

# A 3-D hybrid finite-difference—finite-element viscoelastic modelling of seismic wave motion

Martin Galis,<sup>1,2</sup> Peter Moczo<sup>1,2</sup> and J. Kristek<sup>1,2</sup>

<sup>1</sup>Faculty of Mathematics, Physics and Informatics, Comenius University, Mlynska dolina F1, 842 48 Bratislava, Slovak Republic

E-mail: moczo@fmph.uniba.sk

<sup>2</sup>Geophysical Institute, Slovak Academy of Sciences, Dubravska cesta 9, 845 28 Bratislava, Slovak Republic

Accepted 2008 May 26. Received 2008 April 30; in original form 2007 October 4

## SUMMARY

We have developed a new hybrid numerical method for 3-D viscoelastic modelling of seismic wave propagation and earthquake motion in heterogeneous media. The method is based on a combination of the fourth-order velocity–stress staggered-grid finite-difference (FD) scheme, that covers a major part of a computational domain, with the second-order finite-element (FE) method which can be applied to one or several relatively small subdomains. The FD and FE parts causally communicate at each time level in the FD–FE transition zone consisting of the FE Dirichlet boundary, FD–FE averaging zone and FD Dirichlet zone.

The implemented FE formulation makes use of the concept of the global restoring-force vector which significantly reduces memory requirements compared to the standard formulation based on the global stiffness matrix.

The realistic attenuation in the whole medium is incorporated using the rheology of the generalized Maxwell body in a definition equivalent to the generalized Zener body.

The FE subdomains can comprise extended kinematic or dynamic models of the earthquake source or the free-surface topography. The kinematic source can be simulated using the body-force term in the equation of motion. The traction-at-split-node method is implemented in the FE method for simulation of the spontaneous rupture propagation.

The hybrid method can be applied to a variety of problems related to the numerical modelling of earthquake ground motion in structurally complex media and source dynamics.

**Key words:** Numerical solutions; Earthquake dynamics; Site effects; Computational seismology; Wave propagation.

## 1 INTRODUCTION

Although many computational and numerical-modelling methods have been developed so far for seismic wave propagation and earthquake motion, no single method can be considered the most efficient and, at the same time, accurate for all wavefield-medium problem configurations. Each method has its advantages and drawbacks either in computational efficiency or accuracy. Although looking for new and more efficient/accurate methods is desirable, possible and, we believe, necessary, a considerable improvement of the present-day modelling tools can be achieved by combining individual methods in hybrid approaches. In some cases it is advantageous to solve time dependence of the displacement using one method and spatial dependence using some other method. For example, Alexeev & Mikhailenko (1980) combined partial separation of variables and finite-difference (FD) method, Mikhailenko & Korneev (1984) combined finite integral Fourier transform and FD method. In some other cases it is reasonable to split the computational domain into two or more parts and solve each part by a proper method. Several hybrid methods were developed, mainly in 2-D, in an effort to achieve reasonable computational efficiency in applications to relatively complex structural models. They include methods by Ohtsuki & Harumi (1983), Shtivelman (1984, 1985), Van den Berg (1984), Kummer *et al.* (1987), Stead & Helmberger (1988), Kawase (1988), Gaffet & Bouchon (1989), Emmerich (1989, 1992), Fäh (1992), Fäh *et al.* (1993), Rovelli *et al.* (1994), Bouchon & Coutant (1994), Robertsson (1996), Zahradník & Moczo (1996), Moczo *et al.* (1997), Lecomte *et al.* (2004) and Ma *et al.* (2004).

Here we focus on the 3-D viscoelastic modelling of earthquake motion in the heterogeneous medium with, optionally, kinematic (point or finite) or dynamic earthquake source. We combine the fourth-order velocity–stress staggered-grid FD scheme with the second-order finite-element (FE) method.

Being well aware of the recently elaborated powerful spectral-element method (e.g. Komatitsch *et al.* 2005; Chaljub *et al.* 2007; Tromp *et al.* 2008) and ADER-DG method (e.g. Käser & Dumbser 2006; Käser *et al.* 2007; de la Puente *et al.* 2007) we believe that our hybrid

approach can be useful in a variety of problem configurations in wave propagation and source dynamics where it can be computationally efficient and, at the same time, sufficiently accurate.

The FE method more easily incorporates boundary conditions at the free surface and material interfaces compared to the FD method if the free surface or internal interface coincides with a surface of gridpoints. Therefore, the FE method is better suited for simulation of the traction-free condition and rupture propagation than the FD method. On the other hand, a FD scheme can be computationally more efficient on a regular space–time grid for modelling seismic wave propagation—for example, if the seismic wave produced by the dynamically rupturing fault are to be propagated away from the fault. It is therefore, very natural to think of a hybrid combination of the two methods if we want to comprise both the dynamic earthquake source and the wave propagation in the complex heterogeneous medium.

The FD and FE methods were combined in the 2-D modelling. Moczo *et al.* (1997) combined the second-order conventional FD scheme with the second-order FE method for the 2-D viscoelastic *P-SV* modelling of seismic motion in the near-surface sedimentary/topographic structure. Ma *et al.* (2004) combined the fourth-order velocity–stress staggered-grid scheme with the second-order FE method for the 2-D elastic *P-SV* modelling. In our hybrid formulation we also combine the second-order FE scheme with the fourth-order FD scheme.

In the FD–FE transition zone the size of the grid spacing in the FE grid is twice smaller compared to that in the FD grid. Away from the transition zone the size of an element can in principle vary. The twice smaller FE grid spacing is algorithmically the most natural option: any other ratio between the FD and FE grid spacings would make the schemes for the transition zone much more complicated and it is likely that it would produce more numerical noise. Intuitively, in a rough estimate, such a choice seems reasonable given the second- and fourth-order approximations in the FE and FD schemes, respectively. Strictly speaking, however, the spatial sampling does not simply scale with the approximation order. For example, the increase in the approximation order by two does not mean that as much as twice larger grid spacing can be used. This indicates that an appropriately small FE grid spacing may require a FD grid spacing smaller than that usually used by many modellers in the pure fourth-order staggered-grid modelling. This is additionally and independently supported by results obtained by Kristek & Moczo (2006). They indicated by their numerical investigations for the 1-D problem that the fourth-order staggered-grid scheme requires denser spatial sampling than that usually used by many users who consider it approximately twice coarser than that in the second-order conventional schemes.

One other aspect of the spatial sampling is due to the fact that the numerical modelling of the rupture propagation and free-surface topography requires denser spatial sampling compared to that usually used for the wave propagation.

In the paper we first present, in a concise form, the 3-D viscoelastic fourth-order velocity–stress staggered-grid FD formulation. We continue with a more detailed exposition of the FE method formulated using the restoring force. We then briefly characterize the computational domain. The dominant methodological part of the paper is devoted to the FD–FE transition zone which is a core of the hybrid approach. Results of extensive parametric test simulations are then presented to demonstrate numerical behaviour of the transition zone. In order to illustrate possible applications of the hybrid method, we include partial results of simulations of two hypothetical earthquakes near the Grenoble valley in France.

## 2 EQUATION OF MOTION, CONSTITUTIVE LAW, AND FINITE-DIFFERENCE SCHEME

Rheology of a 3-D isotropic viscoelastic medium can be assumed as made of rheologies of two GMB-EK bodies. GMB-EK means generalized Maxwell body as defined by Emmerich & Korn (1987): several classical Maxwell bodies and one Hooke body connected in parallel. One GMB-EK body represents the complex frequency-dependent bulk modulus. The other represents the complex frequency-dependent shear modulus. Note that rheology of the GMB-EK body is identical to that of the generalized Zener body made of several classical Zener bodies connected in parallel. The equivalence was shown by Moczo & Kristek (2005).

The following formulations of the equation of motion and the stress–strain relation are used (Kristek & Moczo 2003; Moczo *et al.* 2007a):

$$\rho \dot{v}_i = \sigma_{ij,j} + f_i \quad (1)$$

and

$$\begin{aligned} \dot{\sigma}_{ij} = & \kappa \dot{\epsilon}_{kk} \delta_{ij} + 2\mu \left( \dot{\epsilon}_{ij} - \frac{1}{3} \dot{\epsilon}_{kk} \delta_{ij} \right) \\ & - \sum_{l=1}^n \left[ \kappa Y_l^\kappa \xi_l^{kk} \delta_{ij} + 2\mu Y_l^\mu \left( \xi_l^{ij} - \frac{1}{3} \xi_l^{kk} \delta_{ij} \right) \right], \end{aligned} \quad (2)$$

$$\dot{\xi}_l^{ij} + \omega_l \xi_l^{ij} = \omega_l \dot{\epsilon}_{ij}; \quad l = 1, \dots, n. \quad (3)$$

Here, in a Cartesian coordinate system  $(x_1, x_2, x_3)$  or  $(x, y, z)$ ,  $i, j, k \in \{1, 2, 3\}$ ,  $\rho(x_i)$  is density,  $\kappa(x_i)$  unrelaxed (elastic) bulk modulus,  $\mu(x_i)$  unrelaxed shear modulus,  $Y_l^\kappa$  and  $Y_l^\mu$  anelastic coefficients,  $\vec{v}(x_i, t)$  particle-velocity vector,  $t$  time,  $\dot{v}_i$  time derivative of the  $i$ th component of the particle-velocity vector,  $\vec{f}(x_i, t)$  body force per unit volume,  $\sigma_{ij}(x_k, t)$  stress tensor,  $\dot{\sigma}_{ij}$  time derivative of the stress tensor,  $\sigma_{ij,j}$  spatial derivative of the stress tensor with respect to  $x_j$ ,  $\dot{\epsilon}_{ij}(x_k, t)$  time derivative of the strain tensor,  $\xi_l^{ij}(x_k, t)$  material-independent anelastic functions (memory variables),  $\omega_l$  angular relaxation frequency for the  $l$ th relaxation mechanism,  $n$  number of relaxation mechanisms, and  $\delta_{ij}$

**Table 1.** Focal and source time function parameters of the point double-couple source used in the numerical tests for the US-12, US-18, FS-12, FS-18, convergence, and contact of two half-spaces problem configurations.

Source parameters				Source-time-function parameters			
Strike $\Phi_S$	Dip $\delta$	Rake $\lambda$	$M_0$	$f_p$	$\gamma_s$	$\Theta$	$t_s$
22.5°	90°	0°	$1 \times 10^{16}$ N m	0.225 Hz	0.25	0.00	0.5 s

Kronecker delta. The equal-index summation convention does not apply to index  $l$ . Coefficients  $Y_l^\kappa$  and  $Y_l^\mu$  are obtained from

$$Y_l^\kappa = \left( \alpha^2 Y_l^\alpha - \frac{4}{3} \beta^2 Y_l^\beta \right) / \left( \alpha^2 - \frac{4}{3} \beta^2 \right) \quad (4)$$

and

$$Y_l^\mu = Y_l^\beta, \quad (5)$$

where  $l = 1, \dots, n$ ,  $\alpha = [(\kappa + \frac{4}{3}\mu)/\rho]^{1/2}$  and  $\beta = (\mu/\rho)^{1/2}$  are elastic  $P$ - and  $S$ -wave velocities. Anelastic coefficients  $Y_l^\alpha$  and  $Y_l^\beta$  are obtained from measured/desired quality factor values  $Q_\alpha$  and  $Q_\beta$  using the system of equations

$$Q_v^{-1}(\tilde{\omega}_k) = \sum_{l=1}^n \frac{\omega_l \tilde{\omega}_k + \omega_l^2 Q_v^{-1}(\tilde{\omega}_k)}{\omega_l^2 + \tilde{\omega}_k^2} Y_l^\nu; \quad k = 1, \dots, 2n-1; \quad \nu \in \{\alpha, \beta\}. \quad (6)$$

System (6) can be solved using the least-square method. For modelling constant or almost constant  $Q(\omega)$  it is reasonable to sample the frequency range of interest with at least  $\omega_l/\omega_{l-1} = 10$ . Frequencies  $\tilde{\omega}_k$  may be chosen as  $\tilde{\omega}_1 = \omega_1$ ,  $\tilde{\omega}_{2n-1} = \omega_n$ , and  $\tilde{\omega}_k/\tilde{\omega}_{k-1} = 5$ .

If the unrelaxed moduli  $\kappa$  and  $\mu$  or, equivalently, elastic velocities  $\alpha$  and  $\beta$  are not known, and, instead, phase velocities  $\alpha(\omega_r)$  and  $\beta(\omega_r)$  at certain frequency  $\omega_r$  are known from measurements, the unrelaxed quantities can be determined from anelastic coefficients  $Y_l^\alpha$  and  $Y_l^\beta$ , and velocities  $\alpha(\omega_r)$  and  $\beta(\omega_r)$ , assuming the rheology of the GMB-EK. For more details see Moczo *et al.* (1997, 2007a).

The FD scheme solving eqs (1)–(3) is the 3-D fourth-order velocity–stress staggered-grid FD scheme presented by Moczo *et al.* (2002, 2004, 2007a,b), Kristek *et al.* (2002), and Kristek & Moczo (2003). Here we only note that the smooth and discontinuous heterogeneity of the viscoelastic medium is accounted for by effective grid material parameters assigned to the grid positions and evaluated as integral volume arithmetic (for density) and harmonic (for viscoelastic moduli) averages. A material discontinuity can intersect a grid cell.

In Fig. 1, we show the spatial distribution of the material and field quantities in the staggered grid. Because the coarse spatial distribution is not applied in the FD–FE transition zone the figure shows a grid cell with all anelastic functions. The figure should help to understand the FD–FE communication in the FD–FE transition zone which is described later. Note that Fig. 1 shows discrete grid quantities for which we use symbols different than for the continuous quantities.

### 3 THE 3-D SECOND-ORDER DISPLACEMENT RESTORING-FORCE FINITE-ELEMENT SCHEME

We use the second-order FE scheme for an isotropic viscoelastic medium. Instead of the standard FE scheme with the global stiffness matrix we use the concept of the restoring-force vector (Frazier & Petersen 1974; Archuleta 1976).

Because the FE scheme with the restoring-force vector is, as far as we know, not so well known or documented in the seismological literature and because we have to explain the incorporation of the GMB-EK rheology in the FE formulation, here we briefly outline the derivation of the FE scheme with the restoring-force vector from the Galerkin formulation of the discretized variational form of the equation of motion for one element  $e$ . A detailed explanation of the concept can be found in Moczo *et al.* (2007a). The equation is

$$\begin{aligned} \int_{\Omega^M} s_k \rho s_l \det \mathbf{J} d\Omega \ddot{u}_{il} + \int_{\Omega^M} s_{k,j} \sigma_{ij} \det \mathbf{J} d\Omega \\ - \int_{\Omega^M} s_k f_i \det \mathbf{J} d\Omega - \int_{\Gamma_N} s_k h_i^e d\Gamma = 0; \end{aligned} \quad (7)$$

$$k, l \in \{1, 2, \dots, L\},$$

where  $s_k$  are the shape functions, indices  $i$  and  $j$  denote spatial coordinates  $(x, y, z)$ ,  $s_{k,j}$  partial spatial derivative of the shape function,  $\rho$  density of the medium in element  $e$ ,  $\sigma_{ij}$  stress tensor,  $f_i$  body force per unit volume,  $\Gamma_N$  part of the boundary of the element with the acting traction  $h_i^e$ ,  $\Omega^M$  master element, and  $L$  the number of nodes in element  $e$ .  $u_{il}$  is the component of the local vector of the discretized displacements at the nodes. The latter vector is

$$\mathbf{u}^e = \begin{bmatrix} \mathbf{u}_x \\ \mathbf{u}_y \\ \mathbf{u}_z \end{bmatrix} = [u_{x1}, \dots, u_{xL}, u_{y1}, \dots, u_{yL}, u_{z1}, \dots, u_{zL}]^T. \quad (8)$$

The integrations in eq. (7) are performed in the master element  $\Omega^M$ , that is, element in the local coordinates. Matrix  $\mathbf{J}$  is the Jacobian of transformation of the master element  $\Omega^M$  from the local coordinates to element  $\Omega^e$  in the global coordinates.

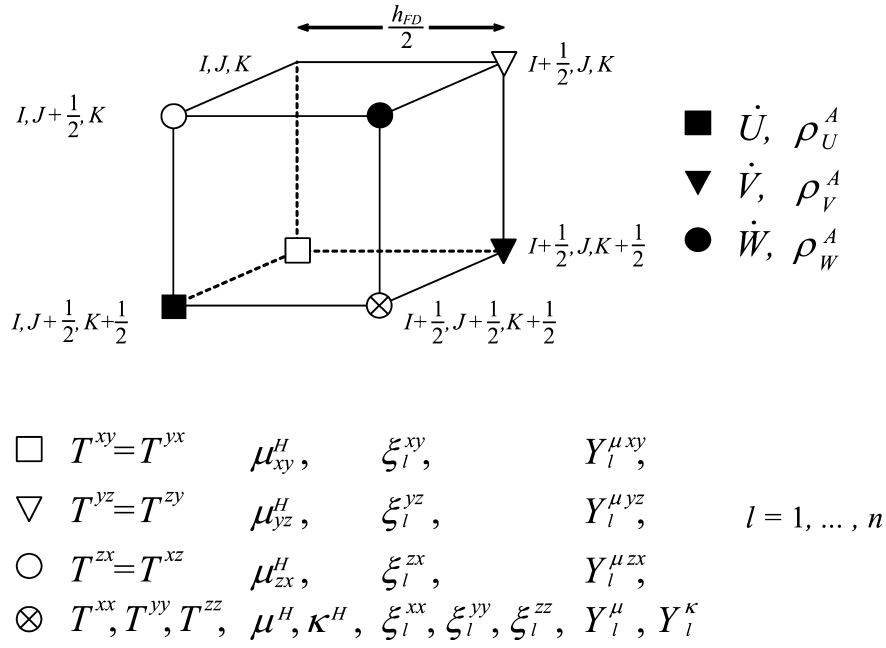


**Figure 1.** A staggered-grid FD cell with positions of particle-velocity components  $\dot{U}$ ,  $\dot{V}$ ,  $\dot{W}$ , stress–tensor components  $T^{xy}$ ,  $T^{yz}$ ,  $T^{zx}$ ,  $T^{xx}$ ,  $T^{yy}$ ,  $T^{zz}$ , anelastic functions  $\xi_l^{xy}$ ,  $\xi_l^{yz}$ ,  $\xi_l^{zx}$ ,  $\xi_l^{xx}$ ,  $\xi_l^{yy}$ ,  $\xi_l^{zz}$ , effective elastic bulk and shear moduli  $\kappa^H$ ,  $\mu^H$ ,  $\mu_{xy}^H$ ,  $\mu_{yz}^H$ ,  $\mu_{zx}^H$  and anelastic coefficients  $Y_l^{\mu}$ ,  $Y_l^{\kappa}$ ,  $Y_l^{\mu xy}$ ,  $Y_l^{\mu yz}$ ,  $Y_l^{\mu zx}$ . Indices  $A$  and  $H$  indicate integral volume arithmetic and harmonic averages.

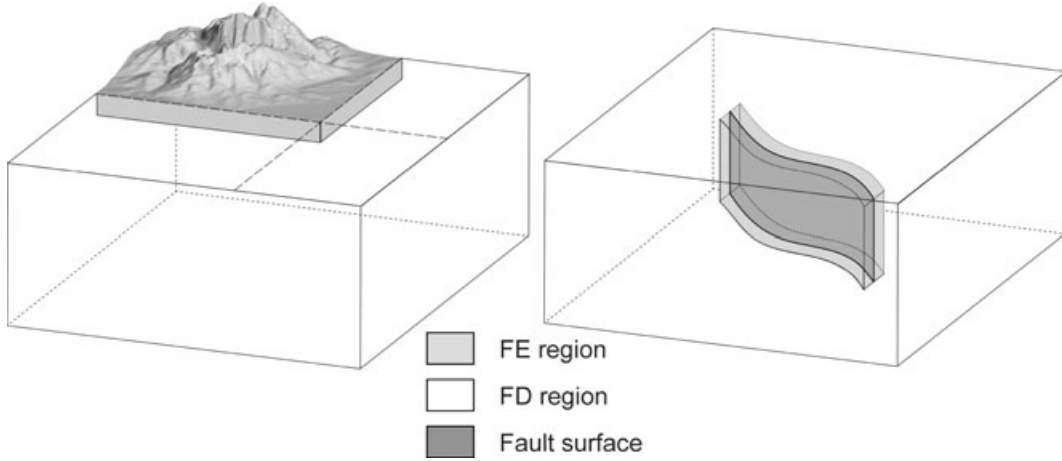


**Figure 2.** Illustration of the computational domain. The FE region can cover a part of the model with a free-surface topography (left-hand side) or a dynamically rupturing surface (right-hand side). The rest of the domain is covered with the FD grid. One computational domain can, in principle, include several FE regions. The latter option is available in the Fortran 95 program 3D.Hybrid.FDFE (available at <http://www.nuquake.eu/Computer.Codes>).

Eq. (7) is a set of 3  $L$  equations and can be written in a matrix form. By applying the standard FE procedure to the first term on the left-hand side of the equation we obtain the well known local mass matrix  $\mathbf{M}^e$ . From the third and fourth terms we obtain a local loading-force vector  $\mathbf{f}^e$ . The application of the standard FE procedure to the second term would lead to the local stiffness matrix (usually denoted by  $\mathbf{K}^e$ ). Here we proceed in other way in order to obtain a local restoring-force vector.

For  $i = x$  we rewrite the second term on the left-hand side of eq. (7) in the form

$$\int_{\Omega^M} s_{k,j} \sigma_{ij} \det \mathbf{J} d\Omega \xrightarrow{i=x} \int_{\Omega^M} [s_{k,x} \sigma_{xx} + s_{k,y} \sigma_{xy} + s_{k,z} \sigma_{xz}] \det \mathbf{J} d\Omega. \quad (9)$$

Considering the vector of shape functions

$$\mathbf{s} = [s_1, \dots, s_L]^T \quad (10)$$

we can define a local vector of the  $x$ -components of the restoring force as

$$\mathbf{r}_x = - \int_{\Omega^M} (\mathbf{s}_{,x} \sigma_{xx} + \mathbf{s}_{,y} \sigma_{xy} + \mathbf{s}_{,z} \sigma_{xz}) \det \mathbf{J} d\Omega. \quad (11)$$

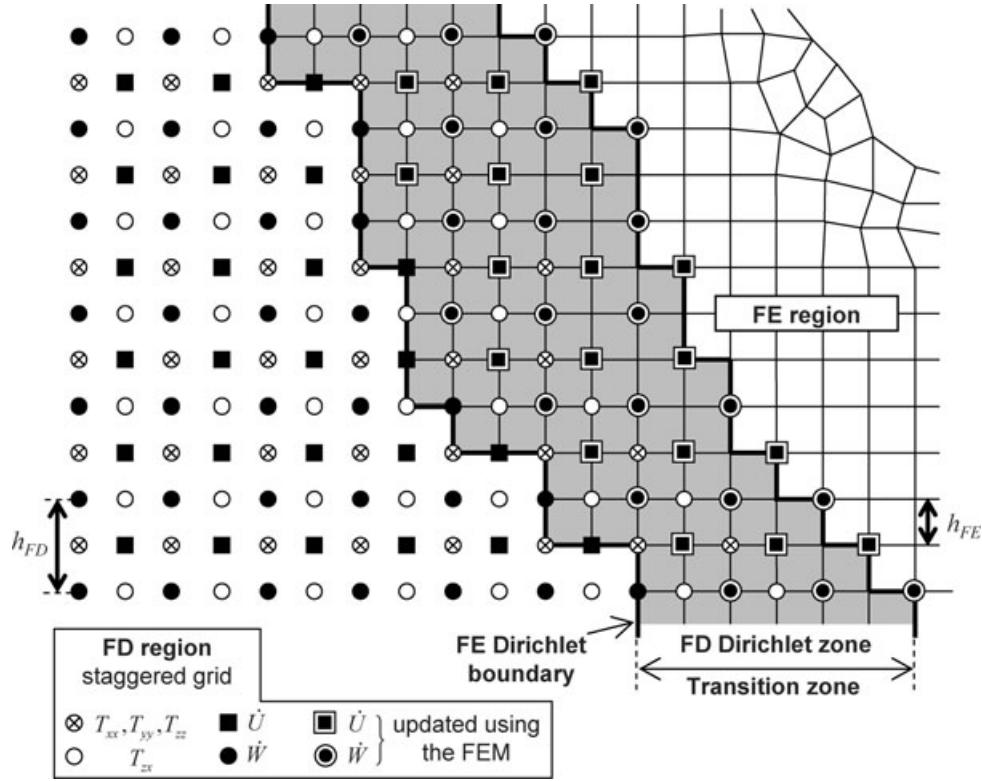


**Figure 3.** Illustration of an algorithmically minimal transition zone for the causal FD–FE communication at each time level. For simplicity, only the vertical grid plane with the  $x$ - and  $z$ -components of the particle velocity,  $\dot{U}$  and  $\dot{W}$ , normal stress–tensor components,  $T_{xx}$ ,  $T_{yy}$  and  $T_{zz}$ , and shear stress–tensor component  $T_{zx}$  is shown (compare with Fig. 1).  $h_{FD}$  is the spatial grid spacing in the FD grid.  $h_{FE}$  is the spatial grid spacing in the uniform part of the FE grid in and near the transition zone; the rest of the FE grid can be non-uniform. Note that no special symbol is used to indicate positions of the displacement vector in the FE grid. Each intersection of the grid lines (gridpoint) in the FE region, is a position of all components of the displacement vector.

Analogously for  $i = y$  and  $i = z$  we obtain

$$\mathbf{r}_y = - \int_{\Omega^M} (\mathbf{s}_{,x} \sigma_{xy} + \mathbf{s}_{,y} \sigma_{yy} + \mathbf{s}_{,z} \sigma_{yz}) \det \mathbf{J} \, d\Omega \quad (12)$$

and

$$\mathbf{r}_z = - \int_{\Omega^M} (\mathbf{s}_{,x} \sigma_{xz} + \mathbf{s}_{,y} \sigma_{yz} + \mathbf{s}_{,z} \sigma_{zz}) \det \mathbf{J} \, d\Omega. \quad (13)$$

Then

$$\mathbf{r}^e = \begin{bmatrix} \mathbf{r}_x \\ \mathbf{r}_y \\ \mathbf{r}_z \end{bmatrix} \quad (14)$$

is the local restoring-force vector. A component of the local restoring-force vector,  $\mathbf{r}_{ik}^e$ , represents the  $i$ -component of the force acting at node  $k$  due to elastic forces acting in the element. These elastic forces represent reaction to the current state of deformation of the element. The forces tend to return the element back to the equilibrium.

The stress tensor for the isotropic elastic medium is given by Hooke's law:

$$\begin{aligned} \sigma_{xx} &= (\lambda + 2\mu) \mathbf{s}_{,x}^T \mathbf{u}_x + \lambda \mathbf{s}_{,y}^T \mathbf{u}_y + \lambda \mathbf{s}_{,z}^T \mathbf{u}_z, \\ \sigma_{yy} &= \lambda \mathbf{s}_{,x}^T \mathbf{u}_x + (\lambda + 2\mu) \mathbf{s}_{,y}^T \mathbf{u}_y + \lambda \mathbf{s}_{,z}^T \mathbf{u}_z, \\ \sigma_{zz} &= \lambda \mathbf{s}_{,x}^T \mathbf{u}_x + \lambda \mathbf{s}_{,y}^T \mathbf{u}_y + (\lambda + 2\mu) \mathbf{s}_{,z}^T \mathbf{u}_z, \\ \sigma_{xy} &= \mu (\mathbf{s}_{,y}^T \mathbf{u}_x + \mathbf{s}_{,x}^T \mathbf{u}_y), \\ \sigma_{yz} &= \mu (\mathbf{s}_{,z}^T \mathbf{u}_y + \mathbf{s}_{,y}^T \mathbf{u}_z), \\ \sigma_{xz} &= \mu (\mathbf{s}_{,z}^T \mathbf{u}_x + \mathbf{s}_{,x}^T \mathbf{u}_z). \end{aligned} \quad (15)$$

Using the local mass matrix  $\mathbf{M}^e$ , the local loading-force vector  $\mathbf{f}^e$ , and local restoring-force vector  $\mathbf{r}^e$  we can rewrite eq. (7) in a matrix form

$$\mathbf{M}^e \ddot{\mathbf{u}}^e = \mathbf{r}^e + \mathbf{f}^e. \quad (16)$$

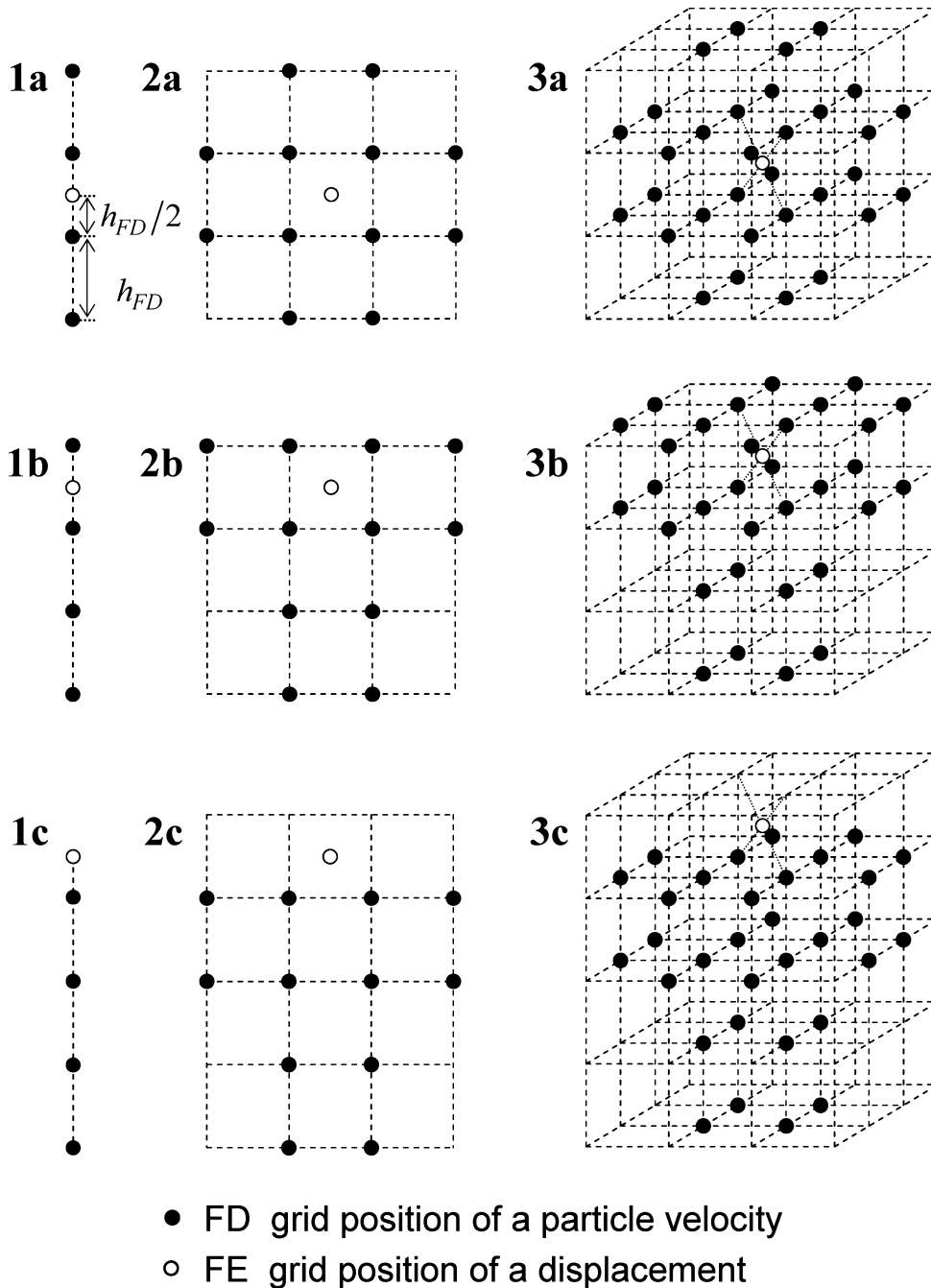


**Figure 4.** Possible spatial configurations of the grid position at which interpolations are necessary. Each of the nine stencils indicates a possible spatial position of the FE-gridpoint (empty circle) of the FE Dirichlet boundary with respect to the FD-grid particle-velocity positions (full circles) used for interpolation. Number 1 (stencils in the left column) refers to the FE-gridpoint located directly at a grid line of the FD-grid values that can be used for the interpolation. The lower-case a, b and c then distinguish three possible configurations along such a grid line. Number 2 refers to the FE-gridpoint located at a grid plane of the FD-grid values that can be used for the interpolation. Number 3 refers to the FE-gridpoint located out of a grid planes and lines of the FD-grid values that can be used for the interpolation.

Following the standard FE procedure to assemble the local systems of equations for all elements in the mesh we obtain a global system of ordinary differential equations

$$\mathbb{M} \ddot{\mathbf{u}} = \mathbf{r} + \mathbf{f}, \quad (17)$$

where  $\mathbb{M}$  is the global mass matrix,  $\ddot{\mathbf{u}}$  global vector of discretized displacements at nodes,  $\mathbf{f}$  global loading-force vector and  $\mathbf{r}$  is the global restoring-force vector.

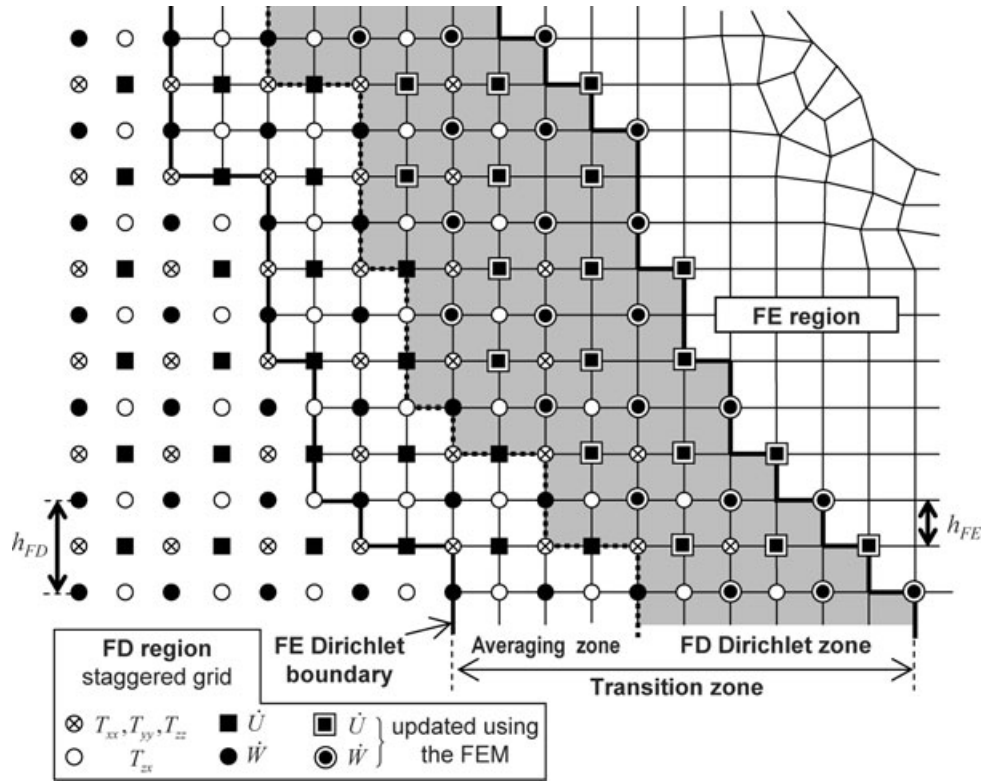


**Figure 5.** Illustration of the FD–FE transition zone used in the hybrid modelling for the causal FD–FE communication at each time level. The difference compared to the algorithmically minimal transition zone consists in a presence of the averaging zone between the FE Dirichlet boundary and FD Dirichlet zone. For simplicity, only the vertical grid plane with the  $x$ - and  $z$ -components of the particle velocity,  $\dot{U}$  and  $\dot{W}$ , normal stress–tensor components,  $T_{xx}$ ,  $T_{yy}$  and  $T_{zz}$ , and shear stress–tensor component  $T_{zx}$  is shown (compare with Fig. 1).  $h_{FD}$  is the spatial grid spacing in the FD grid.  $h_{FE}$  is the spatial grid spacing in the uniform part of the FE grid in and near the transition zone; the rest of the FE grid can be non-uniform. Note that no special symbol is used to indicate positions of the displacement in the FE grid. Each intersection of the grid lines (gridpoint) in the FE region is a position of all components of the displacement vector.

Approximating the second time derivative in eq. (17) by the central-difference formula leads to an explicit FE scheme for updating displacements at the time level  $m + 1$ :

$$u^{(m+1)} = (\Delta t)^2 M^{-1} [r^m + f^m] + 2u^m - u^{(m-1)}. \quad (18)$$

Note that the local vector of the restoring force can be expressed using the local stiffness matrix  $K^e$ :

$$r^e = -K^e \cdot u^e. \quad (19)$$

Substitution of expression (19) into eq. (16) would eventually lead to the standard formulation of the FE method with the global stiffness matrix. This, however, implies that the stability and grid dispersion for the FE scheme with the restoring-force vector are exactly the same as those for the standard FE scheme with the global stiffness matrix.

The main reason for the FE scheme with the global restoring-force vector is reduction of the memory required by the global stiffness matrix  $K$ . The matrix is very sparse. Let  $N_n$  be the total number of nodes in the mesh of the hexahedral elements. We use the so-called HEX8 elements with eight nodes at the corners. Then the total number of elements in matrix  $K$  is  $3N_n \times 3N_n$ , whereas the number of non-zero elements is, approximately,  $3N_n \times 81$ . Because the latter number is considerably smaller than the former one, storing only the non-zero elements means relatively considerable reduction of the memory requirements. At the same time,  $3N_n \times 81$  is still a too large number if we realize that even in the modest 3-D modelling millions to tens of millions of nodes are necessary. In other words, the number of the non-zero elements of the global stiffness matrix poses a serious problem.

The global restoring-force vector  $r$  contains  $3N_n$  values. It is 81 times less than the number of the non-zero elements in the global stiffness matrix. As a consequence, the FE formulation (17) needs considerably smaller memory compared to that required by the standard FE formulation with the global stiffness matrix assuming the same time discretization.

On the other hand the stiffness matrix is time-independent and thus it is computed once at the beginning of computation. The restoring force varies with time, and therefore, it has to be updated at each time level. This means that the restoring force reduces memory requirements but increases computational time.

For completeness note that the stiffness matrix is time-independent only if material parameters are time-independent. If we considered time-dependent material parameters, for example, non-linear behaviour of a medium, the stiffness matrix would vary with time. Such a

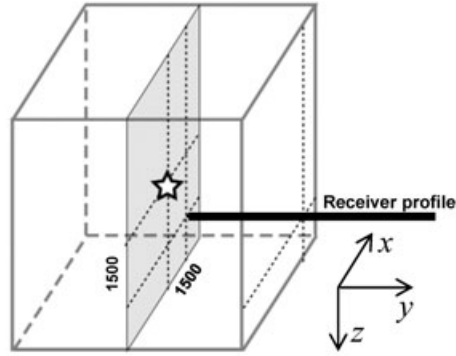
**Unbounded space US-12**

FE Region: **100×100×100 el.**  
(5000×5000×5000 m<sup>3</sup>)

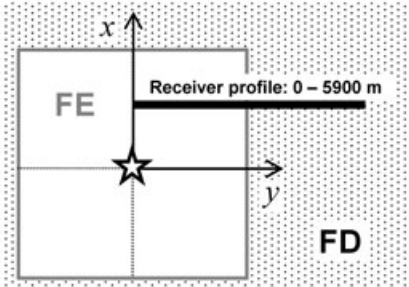
FE sampling:  $\lambda_{\min}/12$  ( $h_{FE} = 50$  m)

FD sampling:  $\lambda_{\min}/6$  ( $h_{FD} = 100$  m)

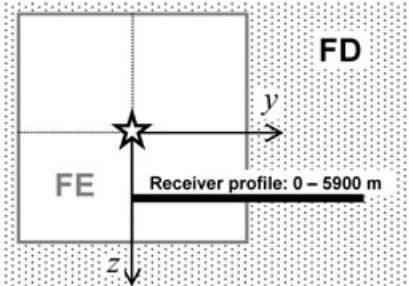
$\lambda_{\min}$  (at 5 Hz) = 600 m



**Horizontal view ( xy-plane )**



**Vertical view ( yz-plane )**

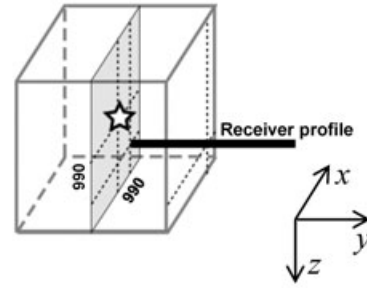
**Unbounded space US-18**

FE Region: **100×100×100 el.**  
(3300×3300×3300 m<sup>3</sup>)

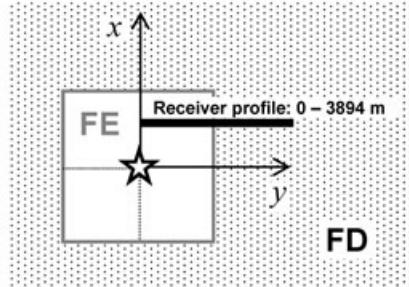
FE sampling:  $\lambda_{\min}/18$  ( $h_{FE} = 33$  m)

FD sampling:  $\lambda_{\min}/9$  ( $h_{FD} = 66$  m)

$\lambda_{\min}$  (at 5 Hz) = 600 m



**Horizontal view ( xy-plane )**



**Vertical view ( yz-plane )**

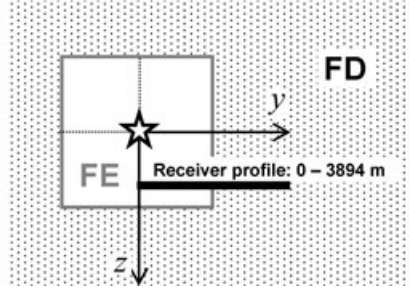


**Figure 6.** Problem configurations for numerical tests of the numerical behaviour of the FD–FE transition zone. A point double-couple source (indicated by a star) and receiver profile (indicated by a thick line) are located in an unbounded homogeneous elastic space. The source is located at the centre of the cube FE region. The FE region is surrounded by the FD region. The receiver profile extends from the FE region through the FD–FE transition zone into the FD region. Two spatial samplings are considered. 12 grid spacings per minimum wavelength are applied in the FE region in the US-12 configuration (left-hand panel) whereas 18 grid spacings per minimum wavelength are applied in the US-18 configuration (right-hand panel). Six and nine grid spacings per minimum wavelength are applied in the FD regions in the two configurations, respectively.

matrix would have to be updated at each time level. In other words, the stiffness-matrix formulation would lose the advantage of smaller computational time.

In a hybrid combination of the FE and FD methods it is necessary that both methods have the same model of realistic attenuation. For the FE scheme we therefore, assume the same GMB-EK rheology as described in the previous section. Because we work with the displacement



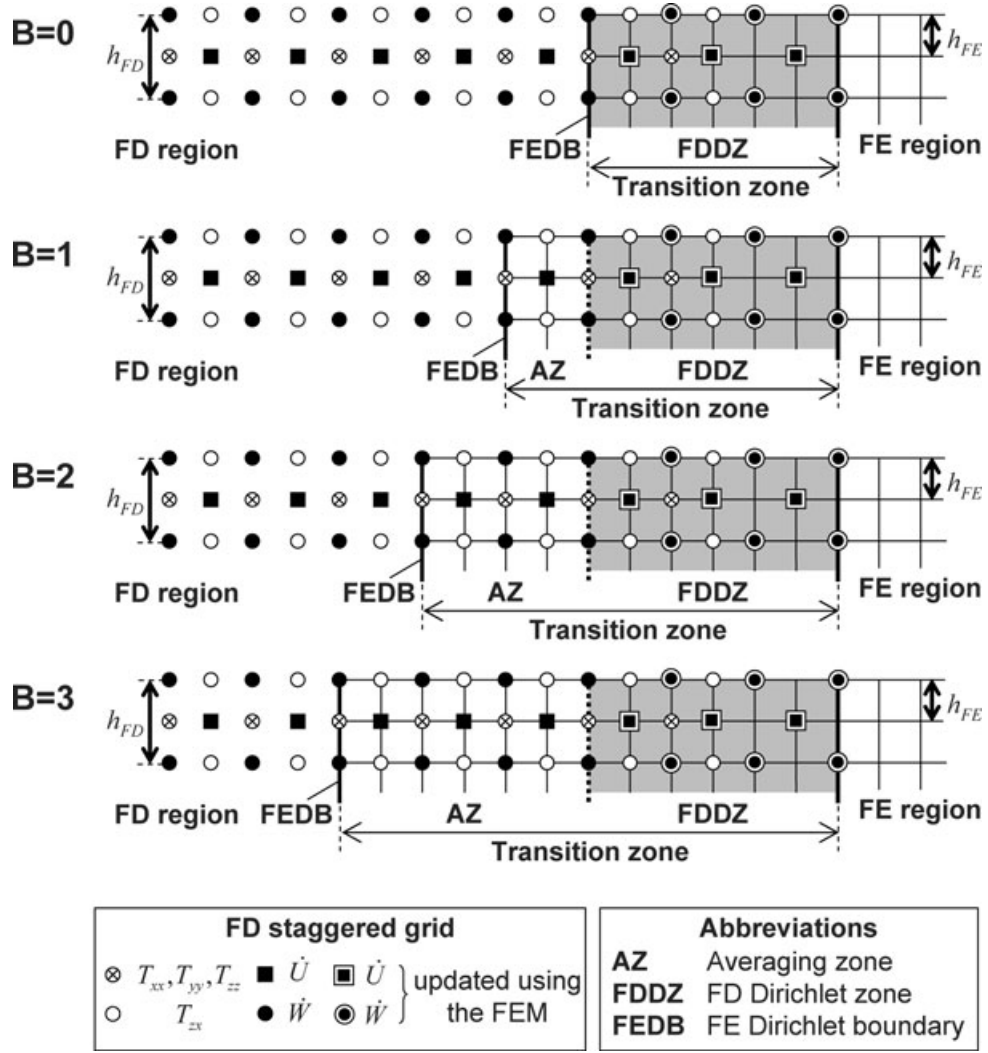


**Figure 7.** For each problem configuration shown in Fig. 6 numerical simulations were performed for four different FD–FE transition zones. The four zones are illustrated using simple geometry here.  $B = 0$  corresponds to the algorithmically minimal transition zone with no averaging zone AZ.  $B = 1, 2, 3$  correspond to the transition zones with different thicknesses of the averaging zone AZ.

formulation, we consider the stress–strain relation in the form (Kristek & Moczo 2003; Moczo *et al.* 2007a)

$$\sigma_{ij} = \kappa \varepsilon_{kk} \delta_{ij} + 2\mu \left( \varepsilon_{ij} - \frac{1}{3} \varepsilon_{kk} \delta_{ij} \right) - \sum_{l=1}^n \left[ \kappa Y_l^\kappa \zeta_l^{kk} \delta_{ij} + 2\mu Y_l^\mu \left( \zeta_l^{ij} - \frac{1}{3} \zeta_l^{kk} \delta_{ij} \right) \right] \quad (20)$$

and

$$\dot{\zeta}_l^{ij} + \omega_l \zeta_l^{ij} = \omega_l \varepsilon_{ij}; \quad l = 1, \dots, n; \quad (21)$$

compare with the analogous relations for the velocity–stress formulation, eqs (2) and (3). Recall that indices  $i, j$  and  $k$  ( $i, j, k \in \{x, y, z\}$ ) are spatial indices, index  $l$  denotes the  $l$ th relaxation mechanism,  $n$  denotes the number of relaxation mechanisms, and the equal-index summation convention does not apply to  $l$ .

Rewrite the stress–strain relation (20) in the form more suitable for the FE implementation:

$$\sigma_{ij} = \sigma_{ij}^E - \sum_{l=1}^n \sigma_{ij}^{A^l}. \quad (22)$$

We split the stress tensor into the elastic and anelastic parts. The elastic part  $\sigma_{ij}^E$  is given by Hooke’s law (15). The anelastic part is determined by a sum of the anelastic terms  $\sigma_{ij}^{A^l}$  for all relaxation frequencies—due to superposition of all relaxation mechanisms. A vector of the anelastic

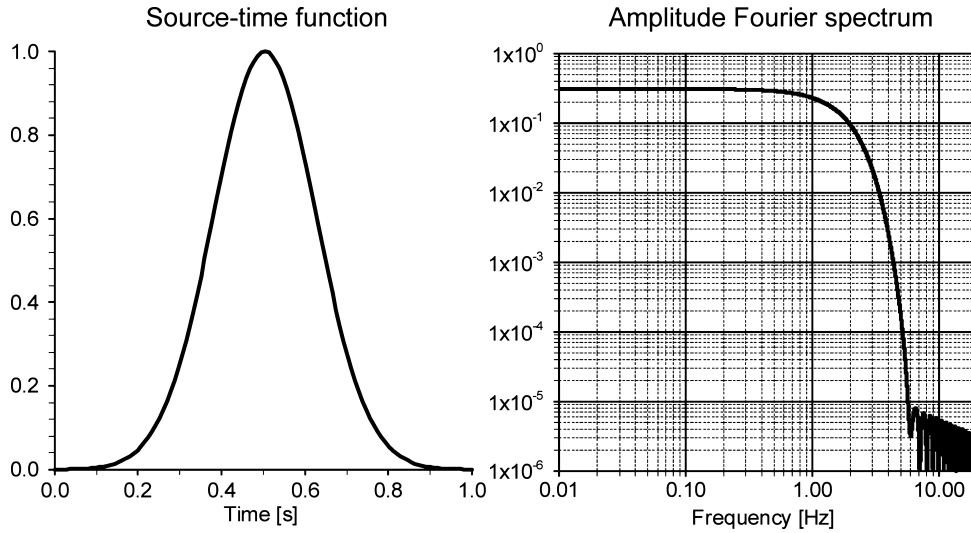


**Figure 8.** Gabor signal used as the source time function in the numerical tests of behaviour of the FD–FE transition zone (left-hand side), and its amplitude Fourier spectrum (right-hand side).

terms  $\sigma_{ij}^{Al}$  can be written as

$$\begin{bmatrix} \sigma_{xx}^{Al} \\ \sigma_{yy}^{Al} \\ \sigma_{zz}^{Al} \\ \sigma_{xy}^{Al} \\ \sigma_{yz}^{Al} \\ \sigma_{xz}^{Al} \end{bmatrix} = \begin{bmatrix} Y_l^+ & Y_l^- & Y_l^- & 0 & 0 & 0 \\ Y_l^- & Y_l^+ & Y_l^- & 0 & 0 & 0 \\ Y_l^- & Y_l^- & Y_l^+ & 0 & 0 & 0 \\ 0 & 0 & 0 & \mu Y_l^\mu & 0 & 0 \\ 0 & 0 & 0 & 0 & \mu Y_l^\mu & 0 \\ 0 & 0 & 0 & 0 & 0 & \mu Y_l^\mu \end{bmatrix} \begin{bmatrix} \zeta_l^{xx} \\ \zeta_l^{yy} \\ \zeta_l^{zz} \\ 2\zeta_l^{xy} \\ 2\zeta_l^{yz} \\ 2\zeta_l^{xz} \end{bmatrix}, \quad (23)$$

where

$$Y_l^+ = \kappa Y_l^\kappa + \frac{4}{3} \mu Y_l^\mu, \quad Y_l^- = \kappa Y_l^\kappa - \frac{2}{3} \mu Y_l^\mu. \quad (24)$$

For solving eq. (21) we use the scheme by Kristek & Moczo (2003). Considering eq. (21) at the time level  $m$ , an approximation of the time derivative using the second-order central-difference formula, and  $\zeta_l^{ij}(m)$  by an arithmetic average of  $\zeta_l^{ij}(m - \frac{1}{2})$  and  $\zeta_l^{ij}(m + \frac{1}{2})$  yields a recurrent formula

$$\zeta_l^{ij}\left(m + \frac{1}{2}\right) = \frac{2\omega_l \Delta t \varepsilon_{ij}(m) + (2 - \omega_l \Delta t) \zeta_l^{ij}\left(m - \frac{1}{2}\right)}{2 + \omega_l \Delta t}. \quad (25)$$

Substituting relation (25) into

$$\zeta_l^{ij}(m) = \frac{1}{2} \left[ \zeta_l^{ij}\left(m - \frac{1}{2}\right) + \zeta_l^{ij}\left(m + \frac{1}{2}\right) \right] \quad (26)$$

we obtain formula for  $\zeta_l^{ij}(m)$ .

The strain–tensor components can be computed using relations

$$\begin{aligned} \varepsilon_{xx} &= \mathbf{s}_{,x}^T \mathbf{u}_x, \\ \varepsilon_{yy} &= \mathbf{s}_{,y}^T \mathbf{u}_y, \\ \varepsilon_{zz} &= \mathbf{s}_{,z}^T \mathbf{u}_z, \\ \varepsilon_{xy} &= \frac{1}{2} (\mathbf{s}_{,y}^T \mathbf{u}_x + \mathbf{s}_{,x}^T \mathbf{u}_y), \\ \varepsilon_{yz} &= \frac{1}{2} (\mathbf{s}_{,z}^T \mathbf{u}_y + \mathbf{s}_{,y}^T \mathbf{u}_z), \\ \varepsilon_{xz} &= \frac{1}{2} (\mathbf{s}_{,z}^T \mathbf{u}_x + \mathbf{s}_{,x}^T \mathbf{u}_z). \end{aligned} \quad (27)$$

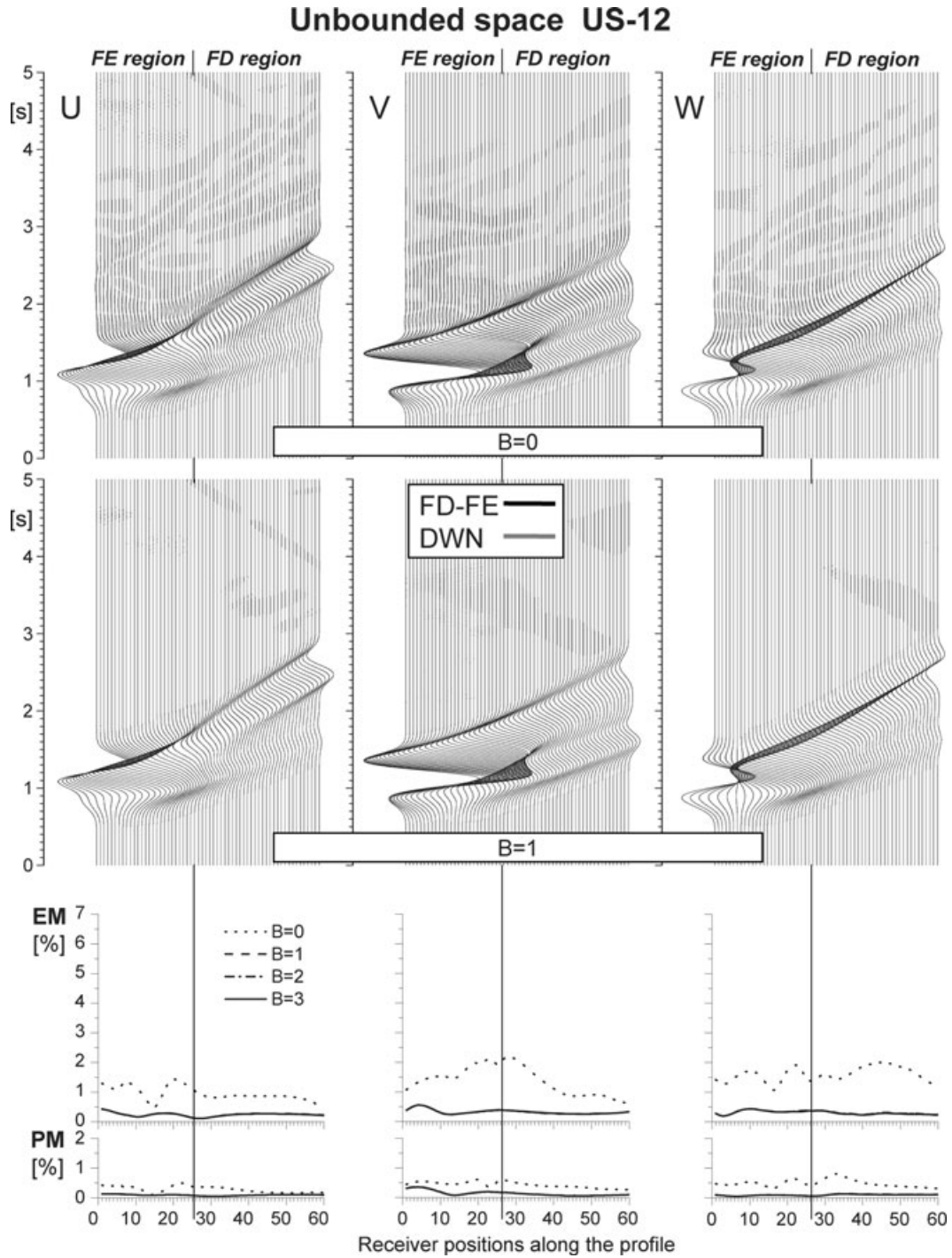


**Figure 9.** Results of the numerical tests—comparison of the FD–FE hybrid synthetics with the DWN solutions for the problem configuration US-12. Left-hand, central and right-hand columns—results for the  $x$ -,  $y$ - and  $z$ -components of the displacement vector (denoted by U, V and W), respectively. Top panel: FD–FE and DWN synthetics along the receiver profile extending from the FE region through the transition zone into the FD region for the algorithmically minimal transition zone ( $B = 0$ ). Middle panel: The same as in the top panel but for the transition zone with the smallest possible averaging zone ( $B = 1$ ). Bottom panel: Envelope (EM) and phase (PM) misfits between the FD–FE and DWN synthetics at all receiver positions for all four considered transition zones ( $B = 0, 1, 2, 3$ ). The vertical line in each column indicates position of the FE Dirichlet boundary.

The local restoring-force vector was defined by relations (11)–(14). For the stress–strain relation (22), the local restoring-force vector takes form

$$\mathbf{r}_i = \mathbf{r}_i^E - \sum_{l=1}^n \mathbf{r}_i^{Al}; \quad i \in \{x, y, z\}, \quad (28)$$

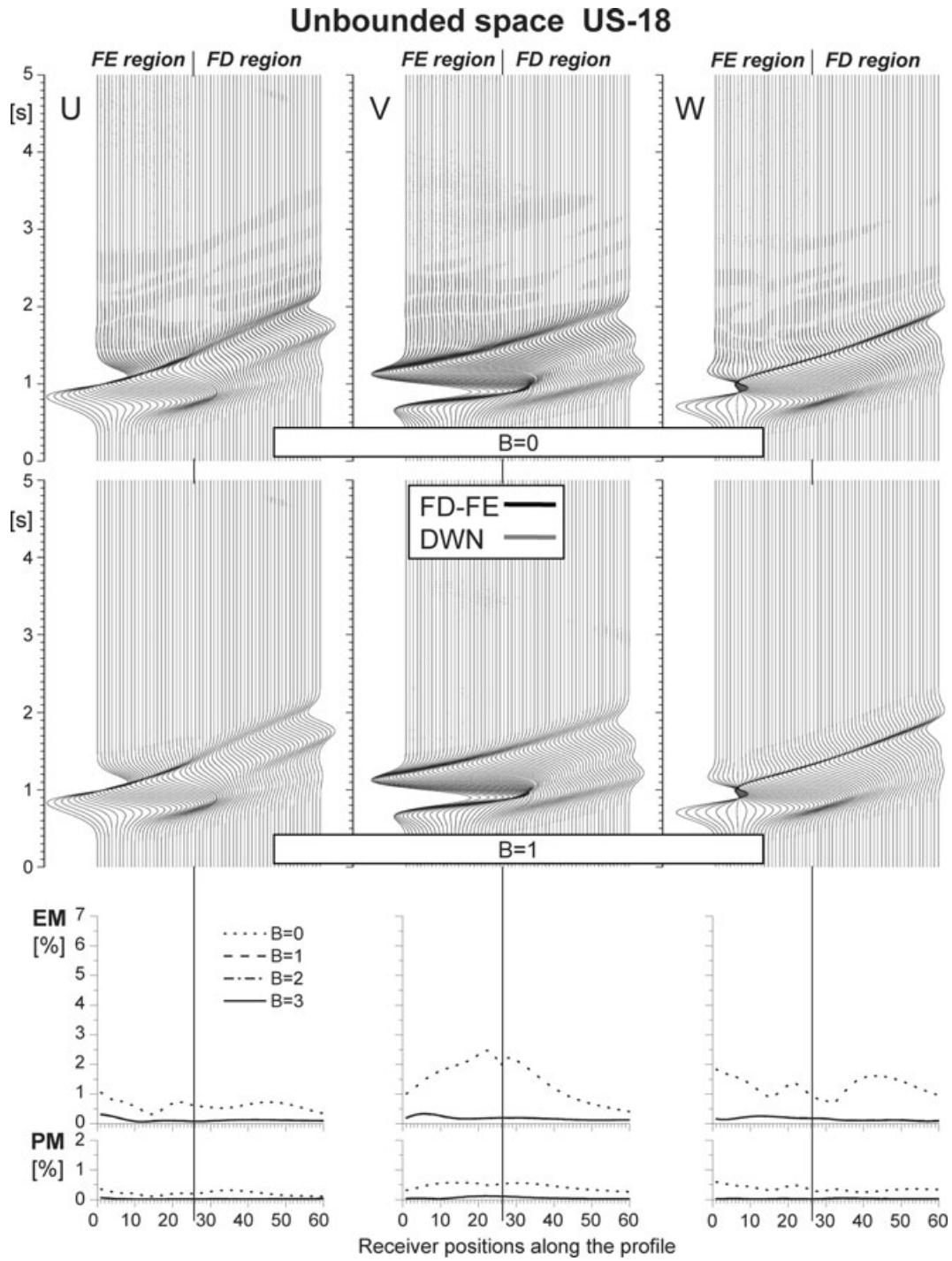


**Figure 10.** The same as in Fig. 9 but for the problem configuration US-18.

where

$$\begin{aligned}
 \mathbf{r}_x^E &= - \int_{\Omega^M} (\mathbf{s}_{,x} \sigma_{xx}^E + \mathbf{s}_{,y} \sigma_{xy}^E + \mathbf{s}_{,z} \sigma_{xz}^E) \det \mathbf{J} \, d\Omega, \\
 \mathbf{r}_y^E &= - \int_{\Omega^M} (\mathbf{s}_{,x} \sigma_{xy}^E + \mathbf{s}_{,y} \sigma_{yy}^E + \mathbf{s}_{,z} \sigma_{yz}^E) \det \mathbf{J} \, d\Omega, \\
 \mathbf{r}_z^E &= - \int_{\Omega^M} (\mathbf{s}_{,x} \sigma_{xz}^E + \mathbf{s}_{,y} \sigma_{yz}^E + \mathbf{s}_{,z} \sigma_{zz}^E) \det \mathbf{J} \, d\Omega,
 \end{aligned} \tag{29}$$

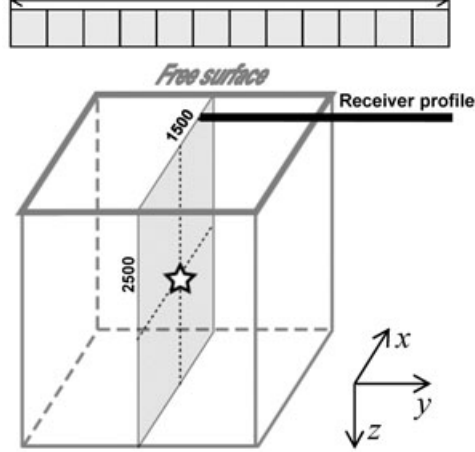
# Free surface

# FS-12

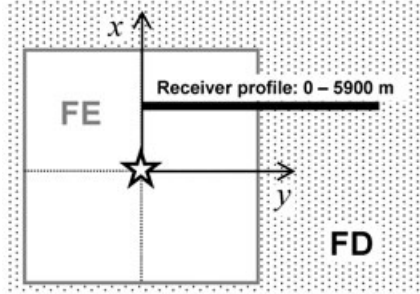
FE Region: **100×100×100 el.**  
(5000×5000×5000 m<sup>3</sup>)

FE sampling:  $\lambda_{\min}/12$  ( $h_{FE} = 50$  m)  
FD sampling:  $\lambda_{\min}/6$  ( $h_{FD} = 100$  m)

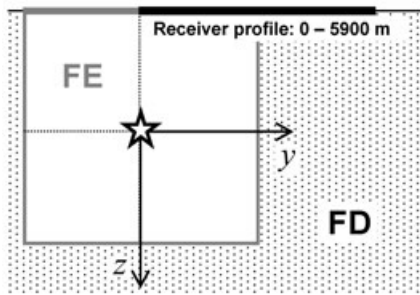
$\lambda_{\min}$  (at 5 Hz) = 600 m



## Horizontal view ( xy-plane )



## Vertical view ( yz-plane )



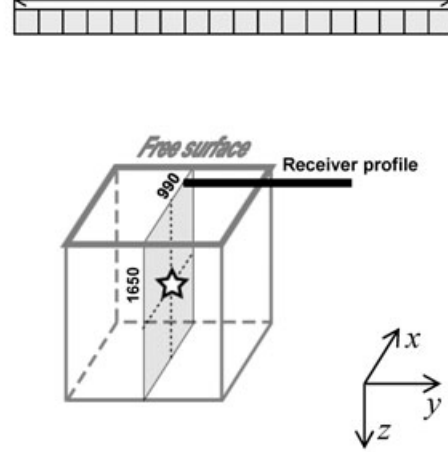
# Free surface

# FS-18

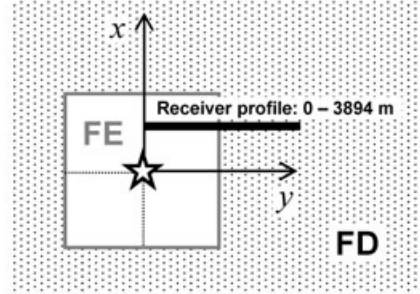
FE Region: **100×100×100 el.**  
(3300×3300×3300 m<sup>3</sup>)

FE sampling:  $\lambda_{\min}/18$  ( $h_{FE} = 33$  m)  
FD sampling:  $\lambda_{\min}/9$  ( $h_{FD} = 66$  m)

$\lambda_{\min}$  (at 5 Hz) = 600 m



## Horizontal view ( xy-plane )



## Vertical view ( yz-plane )

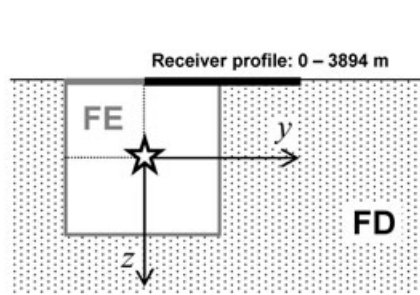


**Figure 11.** Problem configurations for numerical tests of the numerical behaviour of the FD–FE transition zone. A point double-couple source (indicated by a star) is located in a homogeneous half-space. A receiver profile (indicated by a thick line) is located at the planar free surface of the half-space. The source is located at the centre of the cube FE region. The FE region is surrounded by the FD region. The receiver profile at the free surface extends from the FE region through the FD–FE transition zone into the FD region. Two spatial samplings are considered. 12 grid spacings per minimum wavelength are applied in the FE region in the FS-12 configuration (left-hand panel) whereas 18 grid spacings per minimum wavelength are applied in the FS-18 configuration (right-hand panel). Six and nine grid spacings per minimum wavelength are applied in the FD regions in the two configurations, respectively.

and

$$\mathbf{r}_x^{Al} = - \int_{\Omega^M} (\mathbf{s}_{,x} \sigma_{xx}^{Al} + \mathbf{s}_{,y} \sigma_{xy}^{Al} + \mathbf{s}_{,z} \sigma_{xz}^{Al}) \det \mathbf{J} \, d\Omega,$$

$$\mathbf{r}_y^{Al} = - \int_{\Omega^M} (\mathbf{s}_{,x} \sigma_{yx}^{Al} + \mathbf{s}_{,y} \sigma_{yy}^{Al} + \mathbf{s}_{,z} \sigma_{yz}^{Al}) \det \mathbf{J} \, d\Omega,$$

$$\mathbf{r}_z^{Al} = - \int_{\Omega^M} (\mathbf{s}_{,x} \sigma_{zx}^{Al} + \mathbf{s}_{,y} \sigma_{yz}^{Al} + \mathbf{s}_{,z} \sigma_{zz}^{Al}) \det \mathbf{J} \, d\Omega.$$

(30)

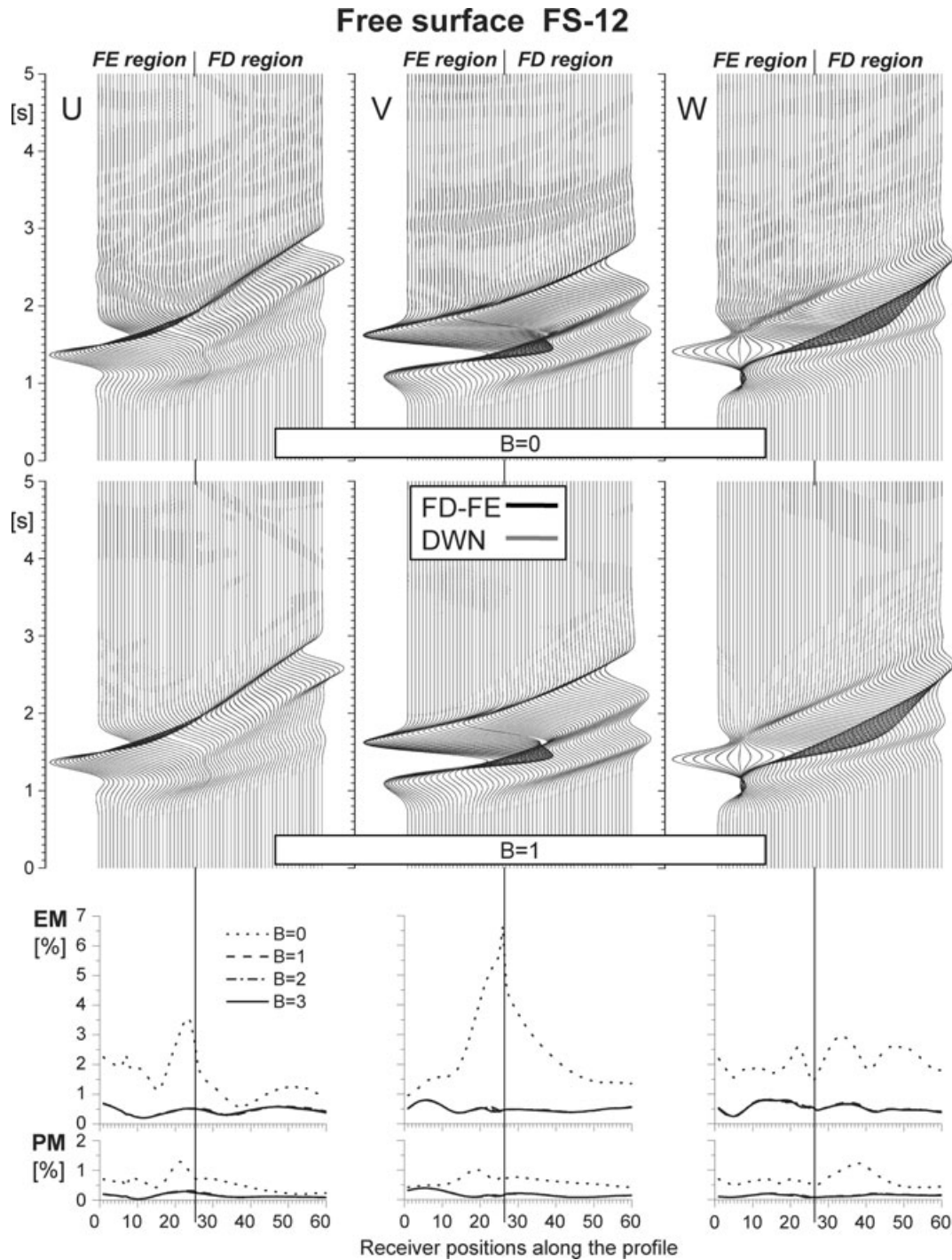


**Figure 12.** The same as in Fig. 9 but for the problem configuration FS-12.

A numerical quadrature for computation of the restoring force requires, in general, anelastic functions at all integration points. The update of the anelastic functions at the time level  $m + \frac{1}{2}$  needs values at the time level  $m - \frac{1}{2}$  that have to be stored in the computer memory. Standard numerical quadratures for the hexahedral element with eight nodes use eight integration points. The corresponding memory requirements are: 8 integration points  $\times$  6 components of the anelastic functions  $\times$   $n$  relaxation frequencies  $\times$  the number of elements in the mesh  $N_e = 48 \times n \times N_e$ . For modelling constant or almost constant  $Q$  we use 4 relaxation frequencies. Then the estimate gives  $192 N_e$ . Obviously, the incorporation of the attenuation dramatically increases the memory requirements; the number of quantities required by the elastic restoring force itself is only  $3N_n$ . Note that the number of nodes  $N_n$  and the number of elements  $N_e$  for large models are approximately the same.

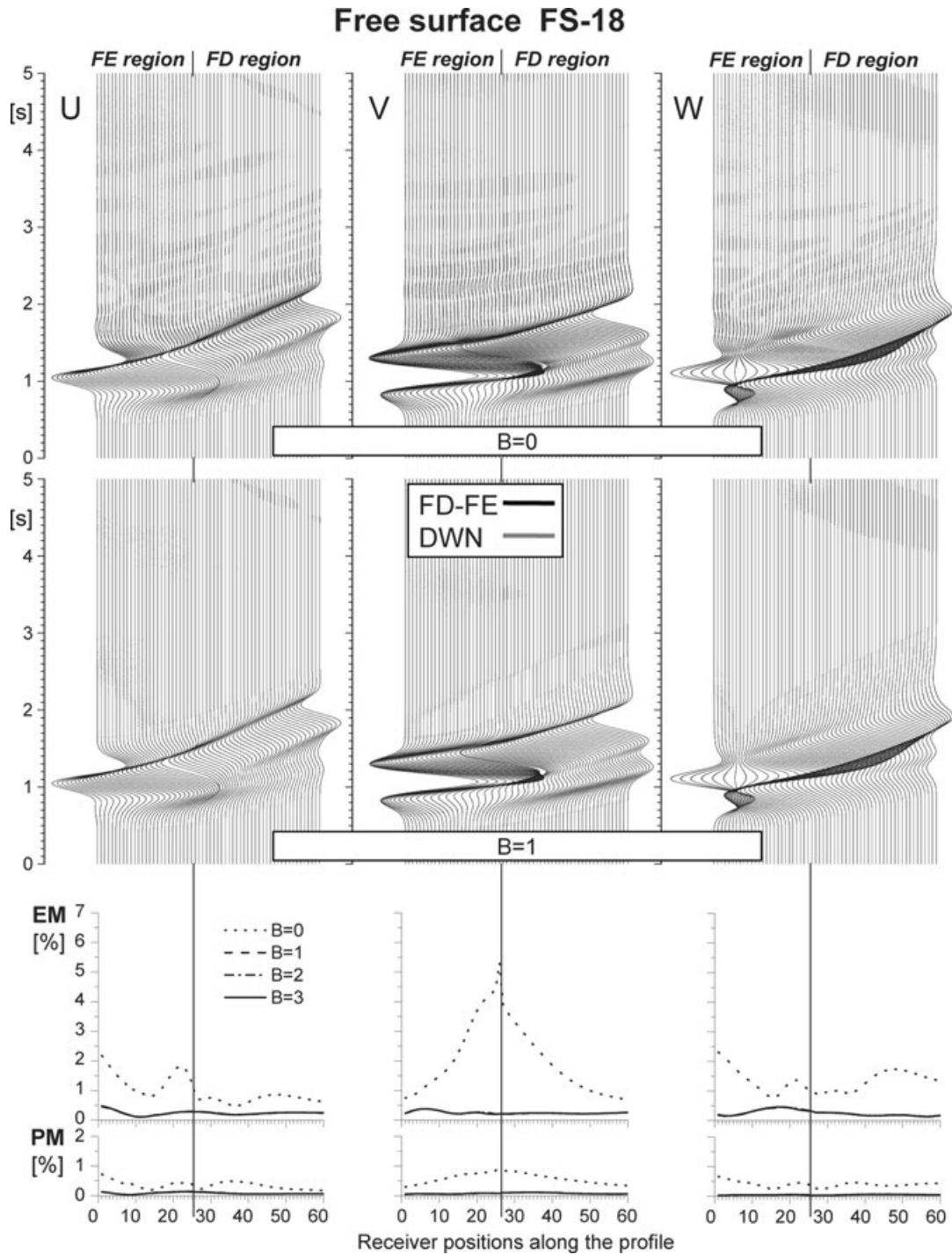


**Figure 13.** The same as in Fig. 9 but for the problem configuration FS-18.

The coarse spatial distribution of the anelastic functions (Day 1998; Graves & Day 2003; Kristek & Moczo 2003) can significantly reduce the additional memory requirements. The techniques are particularly suitable for structured meshes. It is important to consider the FE mesh unstructured. Therefore, we simplify the algorithm and evaluate the anelastic functions only at the centre of an element. This means that for calculation of the anelastic functions we consider constant strain within an element, the strain being located at the element's centre. Then the number of quantities to store is reduced to  $24N_e$ .

We have implemented the traction-at-split-node (TSN) method for a numerical modelling of spontaneous rupture propagation in order to incorporate dynamic source models. The TSN was independently developed by Andrews (1973, 1976a,b, 1999) and Day (1977, 1982). There are some differences in the formulations by Andrews and Day. We closely followed Day's formulation. A detailed exposition of this TSN formulation and implementation can be found in the monograph by Moczo *et al.* (2007a).

# Convergence test

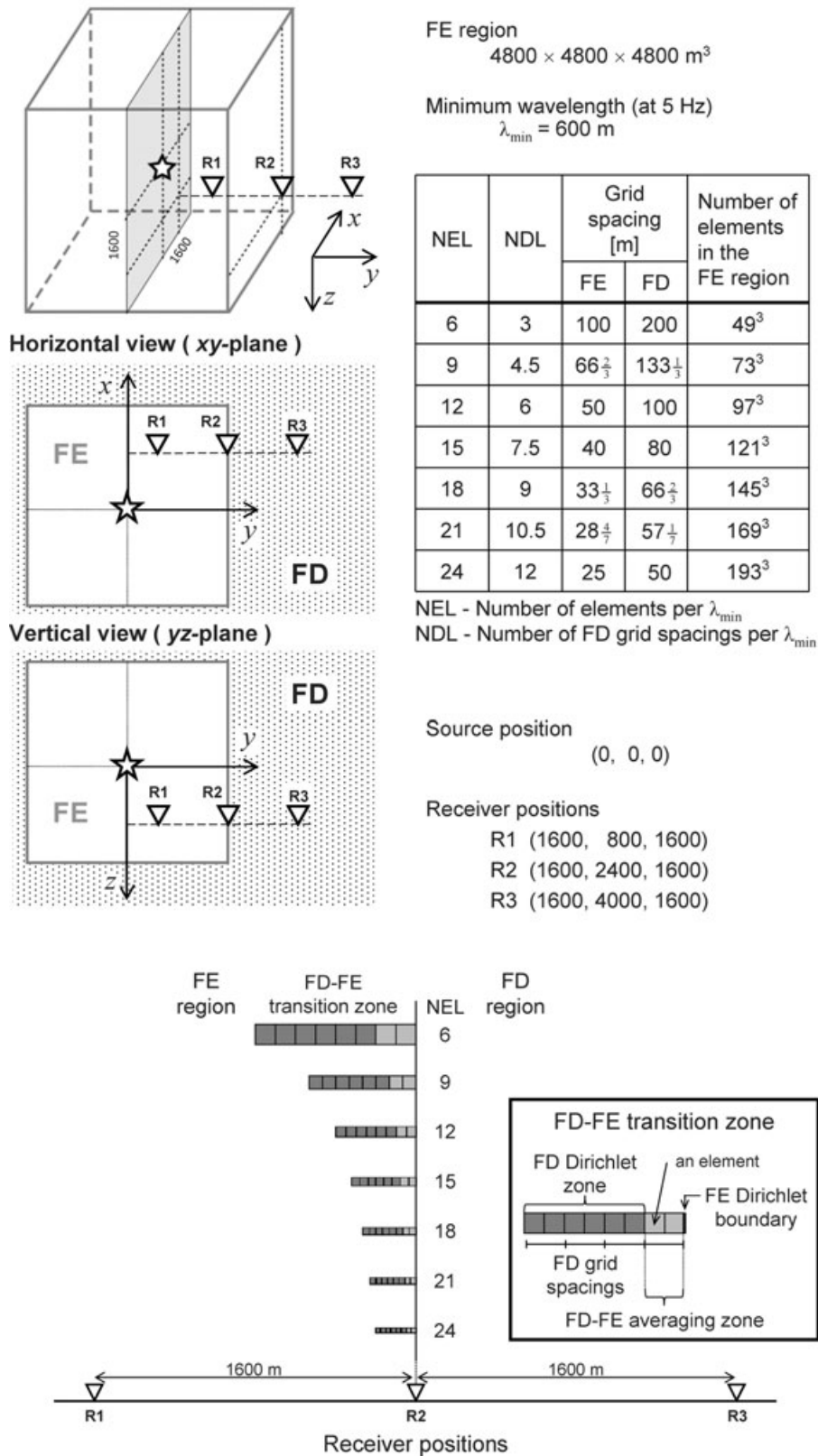


**Figure 14.** Problem configuration and 7 discretizations for the convergence test. The configuration is very similar to that of the US-12 test shown in Fig. 6. A point double-couple source (indicated by a star) and receiver positions (triangles) are located in an unbounded homogeneous elastic space. The numbers of elements and FD grid spacings per  $\lambda_{\min}$ , grid spacings in FE and FD, and the total number of elements in the FE region for each discretization are summarized in the table. The bottom part indicates the sizes of elements, FD–FE transition zones, and receiver positions for all considered discretizations.



## Convergence test

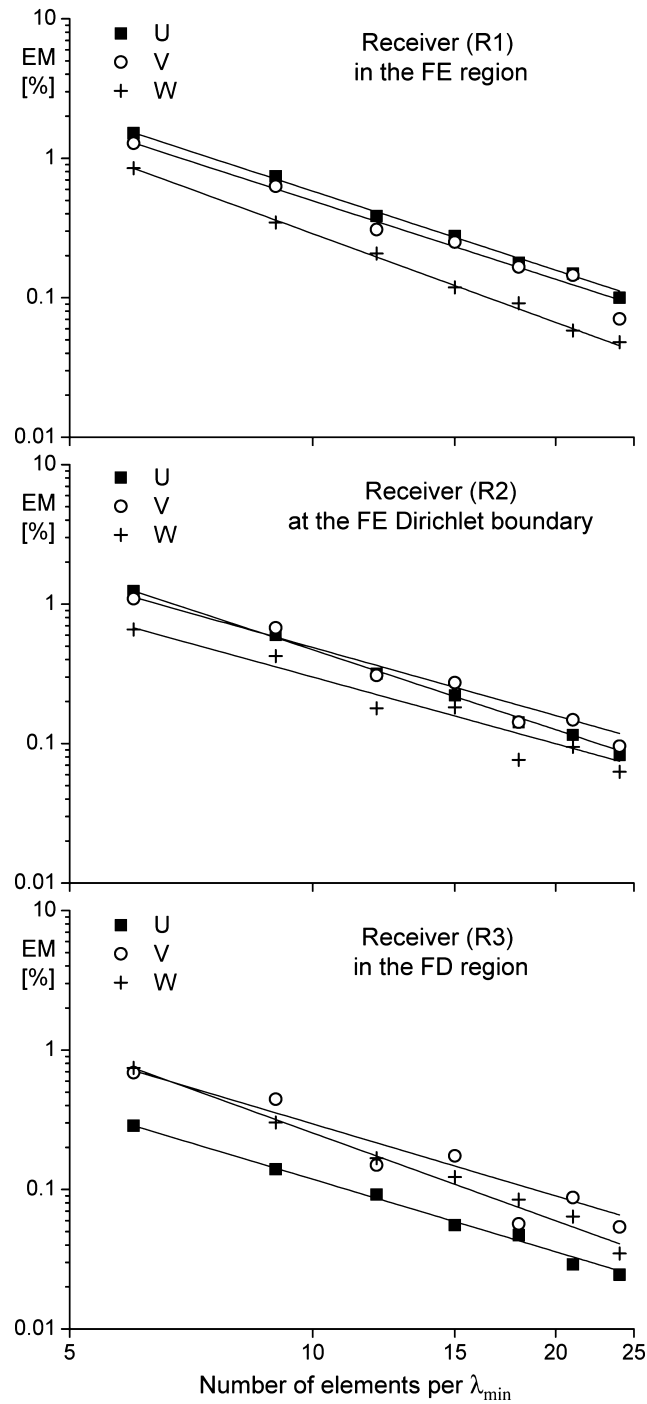


**Figure 15.** Numerical results for the convergence test—envelope misfit (EM) as a function of the number of elements per  $\lambda_{\min}$  for the x-, y- and z-components of the displacement vector (denoted by U, V and W) at three receiver positions.

## 4 COMPUTATIONAL DOMAIN

As already pointed out, the main idea of the hybrid combination of the two methods is to enable efficient numerical simulations considering problem configurations that are as realistic as possible. Such configurations may include a free-surface topography, material heterogeneity as well as a dynamically rupturing fault. Correspondingly, a computational domain of the hybrid FD–FE method may include one or more FE regions that would cover those parts of the model where the free-surface topography or fault have to be considered. As explained in

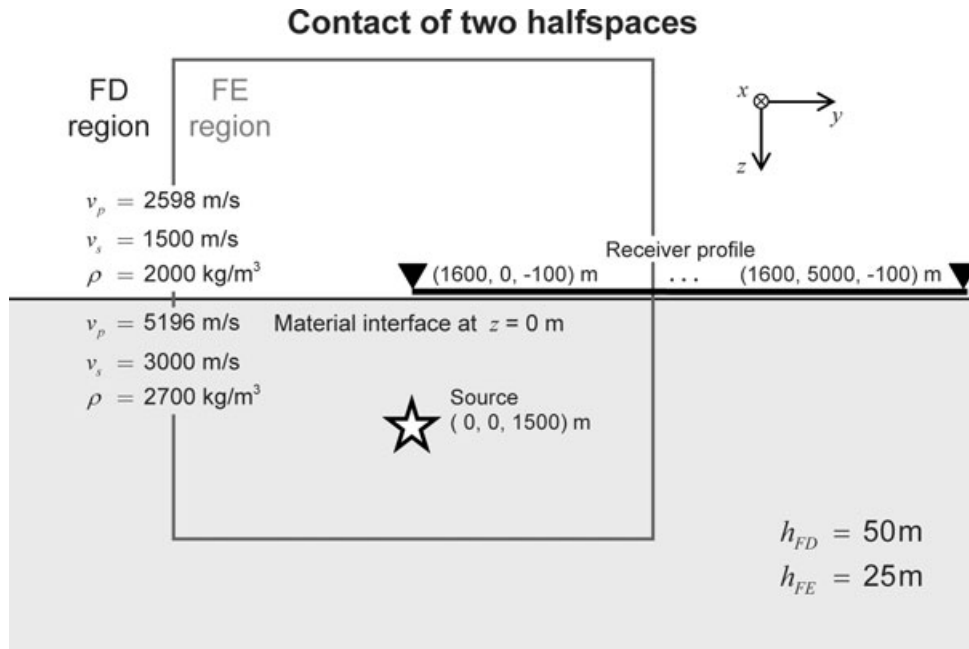


**Figure 16.** Problem configuration in case when a material interface intersects the FD–FE transition zone. The cube FE region is centred around a square of the planar interface between two homogeneous elastic half-spaces. A point double-couple source (indicated by a star) is located in a stiffer half-space. A receiver profile is located in the softer half-space two grid spacings ( $2h_{FD}$ ) from the material interface. The receiver profile extends from the FE region through the FD–FE transition zone into the FD region. The receiver profile is shifted from the vertical plane with the source in the  $x$ -direction by 1600 m.

the introduction, the FE regions should be as small as possible compared to the FD region which should cover a major part of the whole computational domain. The computational domain is schematically illustrated in Fig. 2.

Displacement components in the FE region(s), and particle-velocity and stress–tensor components in the FD region are first updated independently by the FE and FD schemes, respectively. Then the FE regions have to causally communicate at each time level with the FD region. Given the structures of the both schemes, the schemes cannot communicate at a single grid surface. A particular FD–FE transition zone at the contact of the FD and FE regions is necessary for a sufficiently accurate and stable communication. The structure of the transition zone and the algorithm of the FD–FE communication is explained in detail in the next section.

## 5 THE FD–FE TRANSITION ZONE

### 5.1 Principle of the FD–FE communication—an algorithmically minimal transition zone

The FD and FE schemes can communicate with each other at each time level only in the region, where the FD and FE grids overlap—in the transition zone. The shape and size of the transition zone are basically determined by the FD schemes for updating particle-velocity and stress–tensor components. The transition zone is illustrated in Fig. 3. The figure shows an example of a vertical cross-section of a particular transition zone. The zone consists of the FE Dirichlet boundary and FD Dirichlet zone. It is clear that the FE Dirichlet boundary for the second-order displacement FE scheme consists of a single staircase grid surface that has to go through the gridpoints of the FD staggered grid. At the same time, a finite-thickness Dirichlet zone is necessary for the fourth-order velocity–stress staggered-grid FD scheme.

The local thickness and staircase shape of the FD Dirichlet zone are determined by the requirement that the particle velocity at the FD gridpoints located at the FE Dirichlet boundary be calculated using the fourth-order velocity–stress staggered-grid FD scheme for an interior gridpoint. This is possible if relevant stress–tensor components are available. The FD Dirichlet zone has to include those stress–tensor components. Moreover, those stress–tensor components have to be updated by the FD scheme from the particle velocities, because it would be very difficult to calculate the stress–tensor components by the FE schemes at element nodes. For the algorithmic reasons it is reasonable that the relevant particle-velocity components be part of the FD grid.

The FE grid near the transition zone has to be uniform because the staggered grid is uniform.

The algorithm of the causal FD–FE communication in the algorithmically minimal transition zone can be summarized in the following steps. For brevity we use  $U$  for any of the displacement component,  $\dot{U}$  for any particle-velocity component, and  $T$  for any stress–tensor component. Subscripts  $FD$  and  $FE$  refer to the corresponding grids. Lower-case  $m$  denotes a time level.

- (1) Displacements  $U_{FE}(m+1)$  are updated at the gridpoints of the interior FE region (the FE gridpoints except the FE Dirichlet boundary).
- (2) Stress–tensor components  $T(m)$  are updated at the gridpoints of the FD region (including the stress–tensor grid positions inside the FD Dirichlet zone).

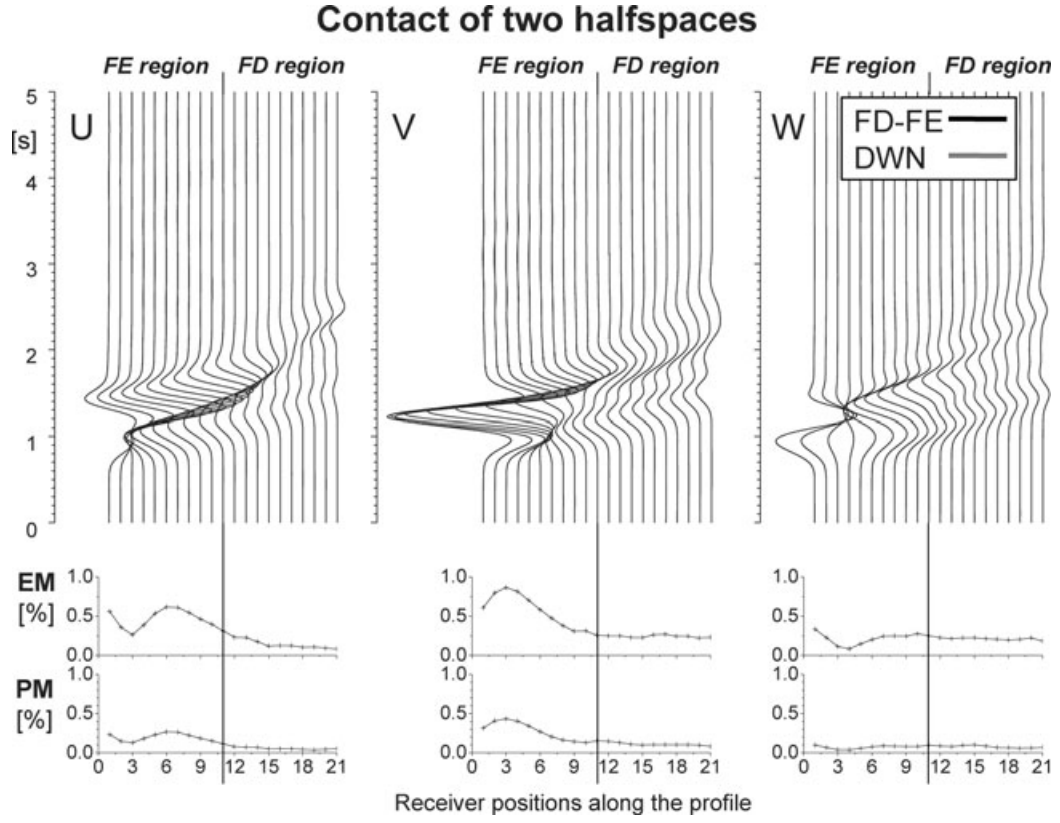


**Figure 17.** Results of the numerical tests—comparison of the FD–FE hybrid synthetics with the DWN solutions for the problem configuration shown in Fig. 16. Left-hand, central and right-hand columns—results for the  $x$ -,  $y$ - and  $z$ -components of the displacement vector (denoted by  $U$ ,  $V$  and  $W$ ), respectively. Top panel: FD–FE and DWN synthetics along the receiver profile extending from the FE region through the transition zone into the FD region. Bottom panel: Envelope (EM) and phase (PM) misfits between the FD–FE and DWN synthetics at all receiver positions. The vertical line in each column indicates position of the FE Dirichlet boundary.

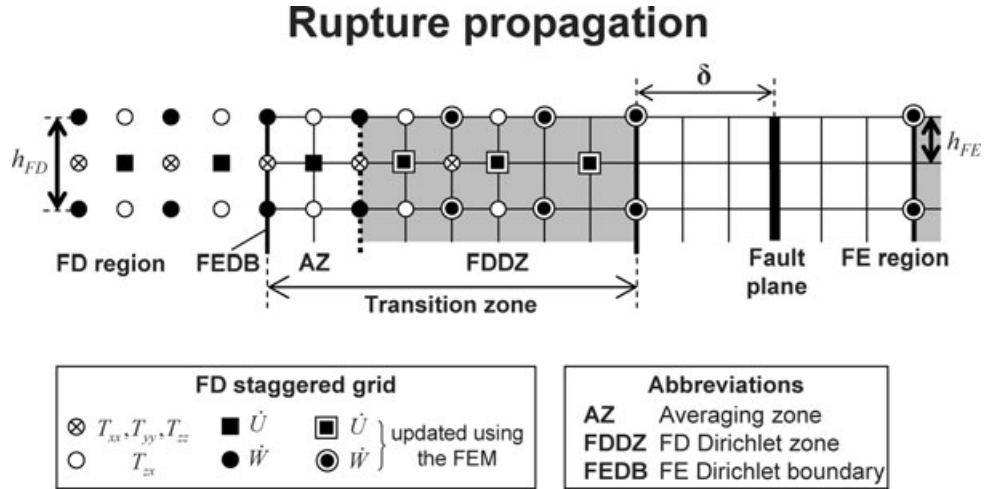


**Figure 18.** Illustration of a position of the fault and the FD–FE transition zone. Distance between the fault plane and FD–FE transition zone is denoted by  $\delta$ . Simulations were performed for six different distances— $\delta \in \{1, 5, 9, 13, 17, 21\} \times h_{FE}$ .

(3) Particle velocities  $\dot{U}_{FD}(m + \frac{1}{2})$  are updated at the gridpoints of the interior FD region.

(4) Particle velocities within the FD Dirichlet zone (at the gridpoints indicated by the double squares and circles in Fig. 3) are updated using the FE displacement values at the same gridpoints:

$$\dot{U}_{FD}\left(m + \frac{1}{2}\right) = \frac{U_{FE}(m + 1) - U_{FE}(m)}{\Delta t}. \quad (31)$$

**Table 2.** Material and computational parameters used in the numerical simulations of the rupture propagation.

$\lambda = \mu$	$v_P$	$v_S$	$\rho$	$h_{\text{FD}}$	$h_{\text{FE}}$	$\Delta t$
34.3 GPa	6050 m s <sup>-1</sup>	3500 m s <sup>-1</sup>	2800 kg m <sup>-3</sup>	50 m	25 m	$1.3875 \times 10^{-3}$ s

*Notes:*  $\lambda$  and  $\mu$  are Lamé elastic parameters,  $v_P$  and  $v_S$  are  $P$ - and  $S$ -wave velocities,  $\rho$  is density,  $h_{\text{FD}}$  is spatial grid spacing in the FD grid,  $h_{\text{FE}}$  is spatial grid spacing in the FE grid and  $\Delta t$  is time step.

**Table 3.** Constitutive parameters of the linear slip-weakening friction law used in the numerical simulations of the rupture propagation.

$\sigma_0$	$\tau_0$	$\mu_u$	$\mu_f$	$d_0$	$S$	$r_{\text{nucl}}$	$\tau_0^{\text{nucl}}$
30.0 GPa	20.0 GPa	0.933	0.250	0.1 m	0.64	300 m	28.14 GPa

*Notes:*  $\sigma_0$  is initial normal traction,  $\tau_0$  is initial shear traction,  $\mu_u$  is static coefficient of friction,  $\mu_f$  is kinematic coefficient of friction,  $d_0$  is characteristic slip-weakening distance,  $S$  is strength parameter,  $r_{\text{nucl}}$  is radius of a circular nucleation zone and  $\tau_0^{\text{nucl}}$  is initial shear traction in the nucleation zone.

(5) Displacements  $U_{\text{FE}}(m+1)$  are updated at the FE Dirichlet boundary using the FE displacements and FD particle velocities at the same gridpoints:

$$U_{\text{FE}}(m+1) = U_{\text{FE}}(m) + \Delta t \dot{U}_{\text{FD}}\left(m + \frac{1}{2}\right). \quad (32)$$

Recall that the FE Dirichlet boundary consists of a single staircase grid surface that goes through the gridpoints of the FD staggered grid. A grid position of the FD staggered grid is a position of either of just one particle-velocity component or one shear stress–tensor component or three normal stress–tensor components or none component. At the same time the symbolic eq. (32) requires all particle-velocity components at a given grid position. Consequently, an interpolation of the missing particle-velocity components is necessary. All possible spatial configurations of the grid positions at which interpolations are necessary are symbolically shown in Fig. 4.

Three along-grid-line configurations, labelled 1a, 1b and 1c in Fig. 4, are possible. Let  $p$  denote a true FD grid index along a grid line in any of the three Cartesian coordinate directions. Then the fourth-order interpolation formulas for the three configurations are, respectively,

$$f_p = \frac{9}{16} \left[ f_{p-\frac{1}{2}} + f_{p+\frac{1}{2}} \right] - \frac{1}{16} \left[ f_{p-\frac{3}{2}} + f_{p+\frac{3}{2}} \right], \quad (33)$$

$$f_p = \frac{5}{16} f_{p-\frac{1}{2}} + \frac{15}{16} f_{p+\frac{1}{2}} - \frac{5}{16} f_{p+\frac{3}{2}} + \frac{1}{16} f_{p+\frac{5}{2}}, \quad (34)$$

$$f_p = \frac{35}{16} f_{p+\frac{1}{2}} - \frac{35}{16} f_{p+\frac{3}{2}} + \frac{21}{16} f_{p+\frac{5}{2}} - \frac{5}{16} f_{p+\frac{7}{2}}. \quad (35)$$

Three in-grid-plane configurations labelled 2a, 2b and 2c in Fig. 4 require more complicated interpolation formulas. Let  $p, q$  denote true FD-grid indices of a grid position in any of grid planes parallel with either of the three Cartesian coordinate planes. Then the fourth-order interpolation formulas for the three configurations are, respectively,

$$\begin{aligned} f_{pq} = & \frac{5}{16} \left[ f_{p-\frac{1}{2}, q-\frac{1}{2}} + f_{p+\frac{1}{2}, q-\frac{1}{2}} + f_{p-\frac{1}{2}, q+\frac{1}{2}} + f_{p+\frac{1}{2}, q+\frac{1}{2}} \right] \\ & - \frac{1}{32} \left[ f_{p-\frac{3}{2}, q-\frac{1}{2}} + f_{p-\frac{3}{2}, q+\frac{1}{2}} + f_{p+\frac{3}{2}, q-\frac{1}{2}} + f_{p+\frac{3}{2}, q+\frac{1}{2}} \right] \\ & + f_{p-\frac{1}{2}, q-\frac{3}{2}} + f_{p-\frac{1}{2}, q+\frac{3}{2}} + f_{p+\frac{1}{2}, q-\frac{3}{2}} + f_{p+\frac{1}{2}, q+\frac{3}{2}} \end{aligned} \quad (36)$$

$$\begin{aligned} f_{pq} = & \frac{3}{16} \left[ f_{p-\frac{1}{2}, q-\frac{1}{2}} + f_{p+\frac{1}{2}, q-\frac{1}{2}} \right] + \frac{1}{2} \left[ f_{p-\frac{1}{2}, q+\frac{1}{2}} + f_{p+\frac{1}{2}, q+\frac{1}{2}} \right] \\ & - \frac{5}{32} \left[ f_{p-\frac{1}{2}, q+\frac{3}{2}} + f_{p+\frac{1}{2}, q+\frac{3}{2}} \right] + \frac{1}{32} \left[ f_{p-\frac{1}{2}, q+\frac{5}{2}} + f_{p+\frac{1}{2}, q+\frac{5}{2}} \right], \\ & - \frac{1}{32} \left[ f_{p-\frac{3}{2}, q-\frac{1}{2}} + f_{p-\frac{3}{2}, q+\frac{1}{2}} + f_{p+\frac{3}{2}, q-\frac{1}{2}} + f_{p+\frac{3}{2}, q+\frac{1}{2}} \right] \end{aligned} \quad (37)$$

$$\begin{aligned} f_{pq} = & \frac{19}{16} \left[ f_{p-\frac{1}{2}, q+\frac{1}{2}} + f_{p+\frac{1}{2}, q+\frac{1}{2}} \right] - \frac{3}{32} \left[ f_{p-\frac{3}{2}, q+\frac{1}{2}} + f_{p+\frac{3}{2}, q+\frac{1}{2}} \right] \\ & - \frac{9}{8} \left[ f_{p-\frac{1}{2}, q+\frac{3}{2}} + f_{p+\frac{1}{2}, q+\frac{3}{2}} \right] + \frac{1}{32} \left[ f_{p-\frac{3}{2}, q+\frac{3}{2}} + f_{p+\frac{3}{2}, q+\frac{3}{2}} \right] \\ & + \frac{21}{32} \left[ f_{p-\frac{1}{2}, q+\frac{5}{2}} + f_{p+\frac{1}{2}, q+\frac{5}{2}} \right] - \frac{5}{32} \left[ f_{p-\frac{1}{2}, q+\frac{7}{2}} + f_{p+\frac{1}{2}, q+\frac{7}{2}} \right] \\ & - \frac{3}{32} \left[ f_{p-\frac{3}{2}, q-\frac{1}{2}} + f_{p-\frac{3}{2}, q+\frac{1}{2}} \right] \end{aligned} \quad (38)$$

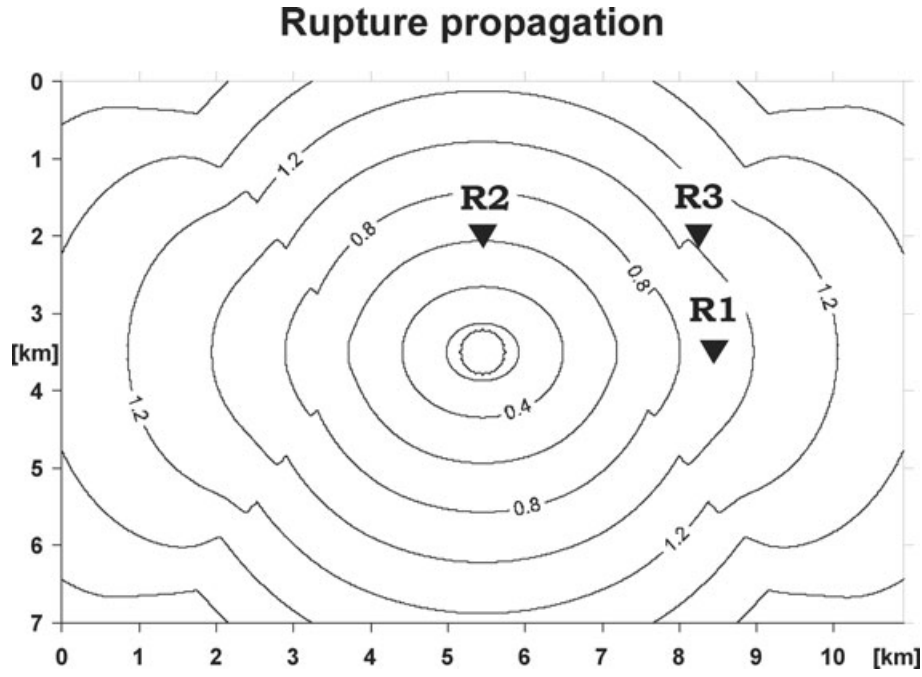


**Figure 19.** Receiver positions on the fault plane and contours of the rupture front. R1 is chosen to be the ‘in-plane-mode’ and R2 ‘antiplane-mode’ receiver. R3 denotes receiver position near the line of the rupture front splitting. The numbers indicate times in seconds for which the rupture front is shown.

Finally, the most complicated but still plausible interpolation formulas are required for three out-of-grid-plane configurations labelled 3a, 3b and 3c in Fig. 4. Let  $p, q, r$  denote true FD-grid indices of a desired FE-grid position. Then the fourth-order interpolation formulas for the three configurations are, respectively,

$$\begin{aligned}
 f_{pqr} = & \frac{11}{64} [f_{p-\frac{1}{2}, q-\frac{1}{2}, r-\frac{1}{2}} + f_{p+\frac{1}{2}, q-\frac{1}{2}, r-\frac{1}{2}} + f_{p-\frac{1}{2}, q+\frac{1}{2}, r-\frac{1}{2}} + f_{p+\frac{1}{2}, q+\frac{1}{2}, r-\frac{1}{2}} \\
 & + f_{p-\frac{1}{2}, q-\frac{1}{2}, r+\frac{1}{2}} + f_{p+\frac{1}{2}, q-\frac{1}{2}, r+\frac{1}{2}} + f_{p-\frac{1}{2}, q+\frac{1}{2}, r+\frac{1}{2}} + f_{p+\frac{1}{2}, q+\frac{1}{2}, r+\frac{1}{2}}] \\
 & - \frac{1}{64} [f_{p-\frac{3}{2}, q-\frac{1}{2}, r-\frac{1}{2}} + f_{p-\frac{3}{2}, q-\frac{1}{2}, r+\frac{1}{2}} + f_{p-\frac{3}{2}, q+\frac{1}{2}, r-\frac{1}{2}} + f_{p-\frac{3}{2}, q+\frac{1}{2}, r+\frac{1}{2}} \\
 & + f_{p+\frac{3}{2}, q-\frac{1}{2}, r-\frac{1}{2}} + f_{p+\frac{3}{2}, q-\frac{1}{2}, r+\frac{1}{2}} + f_{p+\frac{3}{2}, q+\frac{1}{2}, r-\frac{1}{2}} + f_{p+\frac{3}{2}, q+\frac{1}{2}, r+\frac{1}{2}} \\
 & + f_{p-\frac{1}{2}, q-\frac{3}{2}, r-\frac{1}{2}} + f_{p-\frac{1}{2}, q-\frac{3}{2}, r+\frac{1}{2}} + f_{p+\frac{1}{2}, q-\frac{3}{2}, r-\frac{1}{2}} + f_{p+\frac{1}{2}, q-\frac{3}{2}, r+\frac{1}{2}} \\
 & + f_{p-\frac{1}{2}, q+\frac{3}{2}, r-\frac{1}{2}} + f_{p-\frac{1}{2}, q+\frac{3}{2}, r+\frac{1}{2}} + f_{p+\frac{1}{2}, q+\frac{3}{2}, r-\frac{1}{2}} + f_{p+\frac{1}{2}, q+\frac{3}{2}, r+\frac{1}{2}} \\
 & + f_{p-\frac{1}{2}, q-\frac{1}{2}, r-\frac{3}{2}} + f_{p-\frac{1}{2}, q+\frac{1}{2}, r-\frac{3}{2}} + f_{p+\frac{1}{2}, q-\frac{1}{2}, r-\frac{3}{2}} + f_{p+\frac{1}{2}, q+\frac{1}{2}, r-\frac{3}{2}} \\
 & + f_{p-\frac{1}{2}, q-\frac{1}{2}, r+\frac{3}{2}} + f_{p-\frac{1}{2}, q+\frac{1}{2}, r+\frac{3}{2}} + f_{p+\frac{1}{2}, q-\frac{1}{2}, r+\frac{3}{2}} + f_{p+\frac{1}{2}, q+\frac{1}{2}, r+\frac{3}{2}}]
 \end{aligned} \tag{39}$$

$$\begin{aligned}
 f_{pqr} = & \frac{7}{64} [f_{p-\frac{1}{2}, q-\frac{1}{2}, r-\frac{1}{2}} + f_{p+\frac{1}{2}, q-\frac{1}{2}, r-\frac{1}{2}} + f_{p-\frac{1}{2}, q+\frac{1}{2}, r-\frac{1}{2}} + f_{p+\frac{1}{2}, q+\frac{1}{2}, r-\frac{1}{2}}] \\
 & + \frac{17}{64} [f_{p-\frac{1}{2}, q-\frac{1}{2}, r+\frac{1}{2}} + f_{p+\frac{1}{2}, q-\frac{1}{2}, r+\frac{1}{2}} + f_{p-\frac{1}{2}, q+\frac{1}{2}, r+\frac{1}{2}} + f_{p+\frac{1}{2}, q+\frac{1}{2}, r+\frac{1}{2}}] \\
 & - \frac{5}{64} [f_{p-\frac{1}{2}, q-\frac{1}{2}, r+\frac{3}{2}} + f_{p+\frac{1}{2}, q-\frac{1}{2}, r+\frac{3}{2}} + f_{p-\frac{1}{2}, q+\frac{1}{2}, r+\frac{3}{2}} + f_{p+\frac{1}{2}, q+\frac{1}{2}, r+\frac{3}{2}}] \\
 & + \frac{1}{64} [f_{p-\frac{1}{2}, q-\frac{1}{2}, r+\frac{5}{2}} + f_{p+\frac{1}{2}, q-\frac{1}{2}, r+\frac{5}{2}} + f_{p-\frac{1}{2}, q+\frac{1}{2}, r+\frac{5}{2}} + f_{p+\frac{1}{2}, q+\frac{1}{2}, r+\frac{5}{2}}] \\
 & - \frac{1}{64} [f_{p-\frac{3}{2}, q-\frac{1}{2}, r-\frac{1}{2}} + f_{p-\frac{3}{2}, q-\frac{1}{2}, r+\frac{1}{2}} + f_{p-\frac{3}{2}, q+\frac{1}{2}, r-\frac{1}{2}} + f_{p-\frac{3}{2}, q+\frac{1}{2}, r+\frac{1}{2}} \\
 & + f_{p+\frac{3}{2}, q-\frac{1}{2}, r-\frac{1}{2}} + f_{p+\frac{3}{2}, q-\frac{1}{2}, r+\frac{1}{2}} + f_{p+\frac{3}{2}, q+\frac{1}{2}, r-\frac{1}{2}} + f_{p+\frac{3}{2}, q+\frac{1}{2}, r+\frac{1}{2}} \\
 & + f_{p-\frac{1}{2}, q-\frac{3}{2}, r-\frac{1}{2}} + f_{p-\frac{1}{2}, q-\frac{3}{2}, r+\frac{1}{2}} + f_{p+\frac{1}{2}, q-\frac{3}{2}, r-\frac{1}{2}} + f_{p+\frac{1}{2}, q-\frac{3}{2}, r+\frac{1}{2}} \\
 & + f_{p-\frac{1}{2}, q+\frac{3}{2}, r-\frac{1}{2}} + f_{p-\frac{1}{2}, q+\frac{3}{2}, r+\frac{1}{2}} + f_{p+\frac{1}{2}, q+\frac{3}{2}, r-\frac{1}{2}} + f_{p+\frac{1}{2}, q+\frac{3}{2}, r+\frac{1}{2}}]
 \end{aligned} \tag{40}$$

$$\begin{aligned}
f_{pqr} = & \frac{41}{64} [f_{p-\frac{1}{2}, q-\frac{1}{2}, r+\frac{1}{2}} + f_{p+\frac{1}{2}, q-\frac{1}{2}, r+\frac{1}{2}} + f_{p-\frac{1}{2}, q+\frac{1}{2}, r+\frac{1}{2}} + f_{p+\frac{1}{2}, q+\frac{1}{2}, r+\frac{1}{2}}] \\
& - \frac{37}{64} [f_{p-\frac{1}{2}, q-\frac{1}{2}, r+\frac{3}{2}} + f_{p+\frac{1}{2}, q-\frac{1}{2}, r+\frac{3}{2}} + f_{p-\frac{1}{2}, q+\frac{1}{2}, r+\frac{3}{2}} + f_{p+\frac{1}{2}, q+\frac{1}{2}, r+\frac{3}{2}}] \\
& + \frac{21}{64} [f_{p-\frac{1}{2}, q-\frac{1}{2}, r+\frac{5}{2}} + f_{p+\frac{1}{2}, q-\frac{1}{2}, r+\frac{5}{2}} + f_{p-\frac{1}{2}, q+\frac{1}{2}, r+\frac{5}{2}} + f_{p+\frac{1}{2}, q+\frac{1}{2}, r+\frac{5}{2}}] \\
& - \frac{5}{64} [f_{p-\frac{1}{2}, q-\frac{1}{2}, r+\frac{7}{2}} + f_{p+\frac{1}{2}, q-\frac{1}{2}, r+\frac{7}{2}} + f_{p-\frac{1}{2}, q+\frac{1}{2}, r+\frac{7}{2}} + f_{p+\frac{1}{2}, q+\frac{1}{2}, r+\frac{7}{2}}] \\
& - \frac{3}{64} [f_{p-\frac{3}{2}, q-\frac{1}{2}, r+\frac{1}{2}} + f_{p-\frac{3}{2}, q+\frac{1}{2}, r+\frac{1}{2}} + f_{p+\frac{3}{2}, q-\frac{1}{2}, r+\frac{1}{2}} + f_{p+\frac{3}{2}, q+\frac{1}{2}, r+\frac{1}{2}}] \\
& + f_{p-\frac{1}{2}, q-\frac{3}{2}, r+\frac{1}{2}} + f_{p-\frac{1}{2}, q+\frac{3}{2}, r+\frac{1}{2}} + f_{p+\frac{1}{2}, q-\frac{3}{2}, r+\frac{1}{2}} + f_{p+\frac{1}{2}, q+\frac{3}{2}, r+\frac{1}{2}}] \\
& + \frac{1}{64} [f_{p-\frac{3}{2}, q-\frac{1}{2}, r+\frac{3}{2}} + f_{p-\frac{3}{2}, q+\frac{1}{2}, r+\frac{3}{2}} + f_{p+\frac{3}{2}, q-\frac{1}{2}, r+\frac{3}{2}} + f_{p+\frac{3}{2}, q+\frac{1}{2}, r+\frac{3}{2}}] \\
& + f_{p-\frac{1}{2}, q-\frac{3}{2}, r+\frac{3}{2}} + f_{p-\frac{1}{2}, q+\frac{3}{2}, r+\frac{3}{2}} + f_{p+\frac{1}{2}, q-\frac{3}{2}, r+\frac{3}{2}} + f_{p+\frac{1}{2}, q+\frac{3}{2}, r+\frac{3}{2}}]
\end{aligned} \tag{41}$$

We performed an extensive series of numerical tests for the algorithmically minimal FD–FE transition zone illustrated in Fig. 3. Some of the results are shown in the next subsection where they are compared with numerical behaviour of the improved transition zone. The numerical behaviour of the algorithmically minimal FD–FE transition zone is not bad but clearly some slight numerical noise is present in all simulations. The presence of the noise led us to modify the transition zone. The modified zone is presented in the next subsection.

## 5.2 Smooth transition zone with FD–FE averaging

The modification of the algorithmically minimal FD–FE transition zone (shown in Fig. 3) consists in the insertion of the averaging zone between the FE Dirichlet boundary and FD Dirichlet zone. The modified transition zone thus consists of three distinct parts—the FE Dirichlet boundary, FD–FE averaging zone, and FD Dirichlet zone. The modified FD–FE transition zone is illustrated in Fig. 5. The modification also means that the local thickness and staircase shape of the FD Dirichlet zone is determined by requirement that the particle-velocity components at the grid interface between the averaging zone and FD Dirichlet zone be calculated using the fourth-order velocity–stress staggered-grid FD scheme for an interior gridpoint. Note that in the algorithmically minimal zone the same requirement was related to the FE Dirichlet boundary.

Clearly, the question is how thick the averaging zone should be. This can be estimated using numerical tests. Before we present results of the numerical tests we will describe the algorithm of the causal FD–FE communication at each time level in the modified transition zone.

The algorithm of the FD–FE hybrid method can be summarized in the following steps:

- (1) Displacements  $U_{FE}(m+1)$  are updated at the gridpoints of the interior FE region (the FE gridpoints except the FE Dirichlet boundary).
- (2) Stress–tensor components  $T(m)$  are updated at the gridpoints of the FD region including the stress–tensor grid positions inside the FD Dirichlet zone.
- (3) Particle velocities  $\dot{U}_{FD}(m+\frac{1}{2})$  are updated at the gridpoints of the interior FD region including the dashed line (see Fig. 5) between the averaging zone and FD Dirichlet zone.
- (4) Particle velocities  $\dot{U}_{FD}(m+\frac{1}{2})$  within the FD Dirichlet zone (at the gridpoints indicated by double squares and circles in Fig. 5) are updated using the FE displacement values at the same gridpoints:

$$\dot{U}_{FD}\left(m+\frac{1}{2}\right) = \frac{U_{FE}(m+1) - U_{FE}(m)}{\Delta t}. \tag{42}$$

- (5) Particle velocities  $\dot{U}_{FD}(m+\frac{1}{2})$  in the averaging zone, including the dashed line between the averaging and FD Dirichlet zones, are replaced by values obtained by weighted averaging of the FE particle velocities and  $\dot{U}_{FD}(m+\frac{1}{2})$ :

$$\dot{U}_{FD}^w\left(m+\frac{1}{2}\right) = w \frac{U_{FE}(m+1) - U_{FE}(m)}{\Delta t} + (1-w) \dot{U}_{FD}\left(m+\frac{1}{2}\right), \tag{43}$$

where  $w = 1$  at the dashed line between the averaging and FD Dirichlet zones, and  $w = 0$  at the FE Dirichlet boundary. The weighting coefficient linearly changes between the two values over the averaging zone.

- (6) FE displacements  $U_{FE}(m+1)$  in the averaging zone, including the dashed line between the averaging and FD Dirichlet zones, are replaced by averaged values  $U_{FE}^w(m+1)$ :

$$U_{FE}^w\left(m+\frac{1}{2}\right) = w \dot{U}_{FE}\left(m+\frac{1}{2}\right) + (1-w) \dot{U}_{FD}\left(m+\frac{1}{2}\right), \tag{44}$$

$$U_{FE}^w(m+1) = U_{FE}(m) + \Delta t \dot{U}_{FE}^w\left(m+\frac{1}{2}\right). \tag{45}$$

A grid position of the FD staggered grid is a position of either of just one particle-velocity component or one shear stress–tensor component or three normal stress–tensor components or none component. Eq. (44) requires all particle-velocity components at a given grid position. Consequently, an interpolation of the missing particle-velocity components is necessary. The interpolation is the same as that described for the algorithmically minimal transition zone, see eqs (33)–(41).

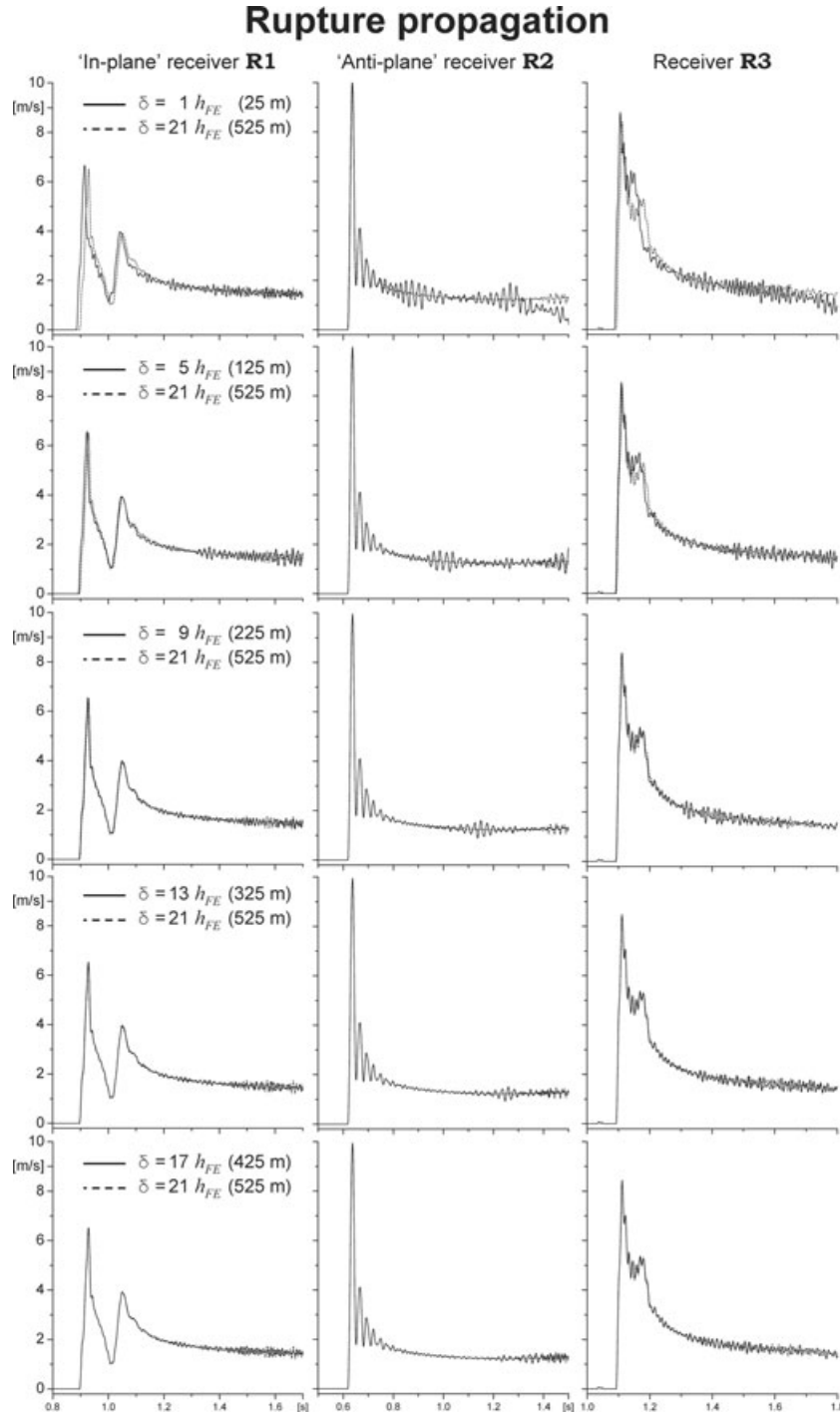


**Figure 20.** Slip-rate time histories obtained in the simulations of the rupture propagation. The value of  $\delta$  in multiples of the FE spatial grid spacing indicates the distance between the rupturing fault plane and FD-FE transition zone. Left-hand, central and right-hand columns: slip-rate histories at receivers R1, R2 and R3, respectively. At each row one of the five solutions,  $\delta \in \{1, 5, 9, 13, 17\} \times h_{FE}$ , is plotted together with the solution for  $\delta = 21 \times h_{FE}$ .

(7) Displacements  $U_{FE}(m + 1)$  are updated at the FE Dirichlet boundary using the FE displacements and FD particle velocities at the same gridpoints:

$$U_{FE}(m + 1) = U_{FE}(m) + \Delta t \dot{U}_{FD} \left( m + \frac{1}{2} \right). \quad (46)$$

Also eq. (46) requires all particle-velocity components at a given FE-grid position. Consequently, an interpolation of the missing particle-velocity components is necessary. Here, however, the weighted-averaged FD particle velocities in the averaging zone are used for the interpolations.

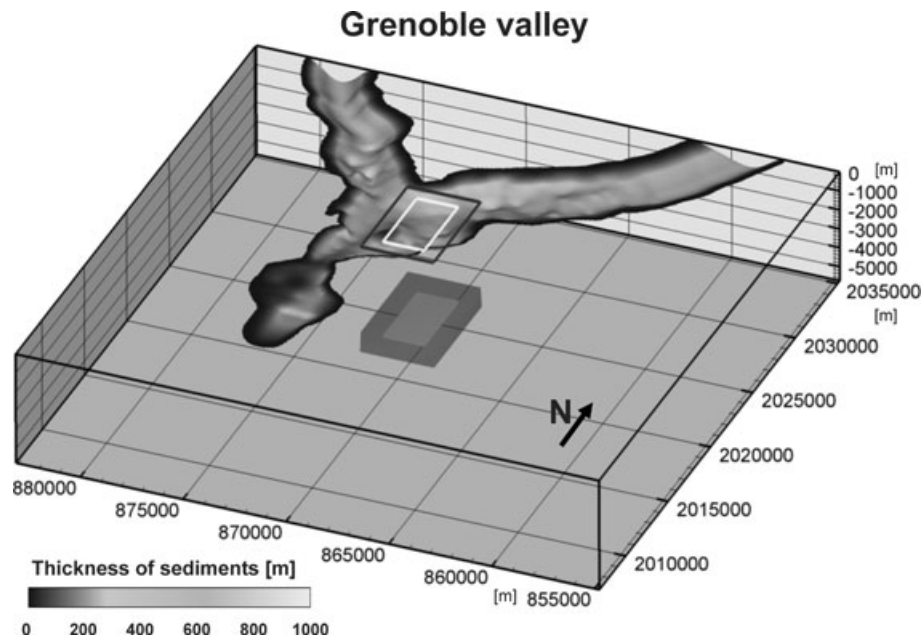


**Figure 21.** Geometrical configuration of the Grenoble valley and dynamically rupturing thrust (horizontal) fault: interface between sediments and bedrock with indication of the sediment thickness, the FE region (dark grey box) covering the ruptured fault area (light grey area inside the dark grey box), projections of the FE region and ruptured fault area onto the flat free surface. The fault is at depth of 5 km.

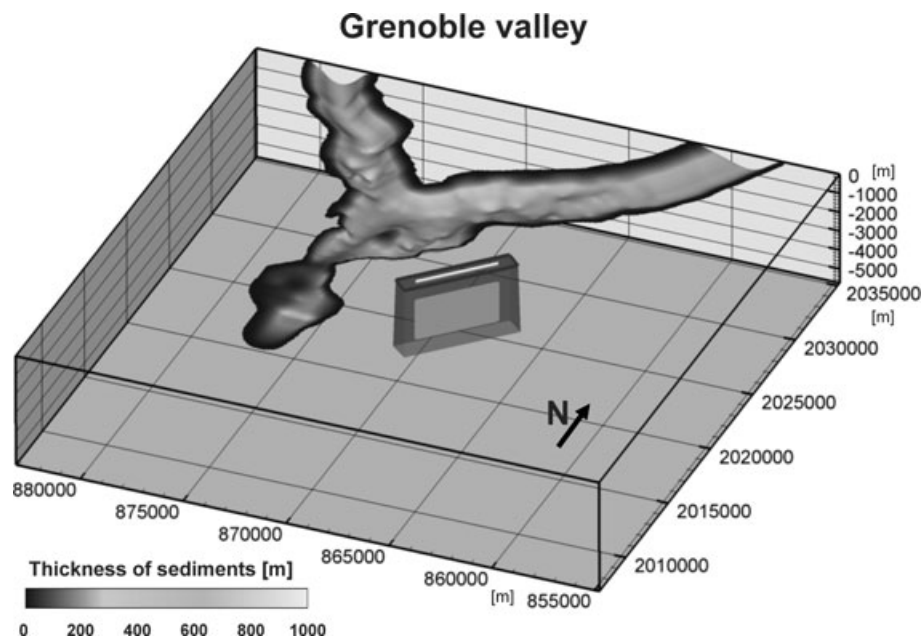


**Figure 22.** Geometrical configuration of the Grenoble valley and dynamically rupturing strike-slip (vertical) fault: interface between sediments and bedrock with indication of the sediment thickness, the FE region (dark grey box) covering the ruptured fault area (light grey area inside the dark grey box), projections of the FE region and ruptured fault area onto the flat free surface. The ruptured fault area reaches depth of 3.5 km.

Note that we introduced the weighted averaging of the FD particle velocities and FE displacements in the averaging zone because we assumed that such a smoothing might improve numerical behaviour of the FD–FE contact.

## 6 NUMERICAL TESTS OF THE ALGORITHMICALLY MINIMAL AND SMOOTH TRANSITION ZONES

We performed extensive numerical tests of the behaviour of the FD–FE transition zone. Clearly, the first question necessary to answer was whether the algorithmically minimal transition zone (Fig. 3) yields stable and sufficiently accurate results. We have not found any indication of



## Grenoble valley

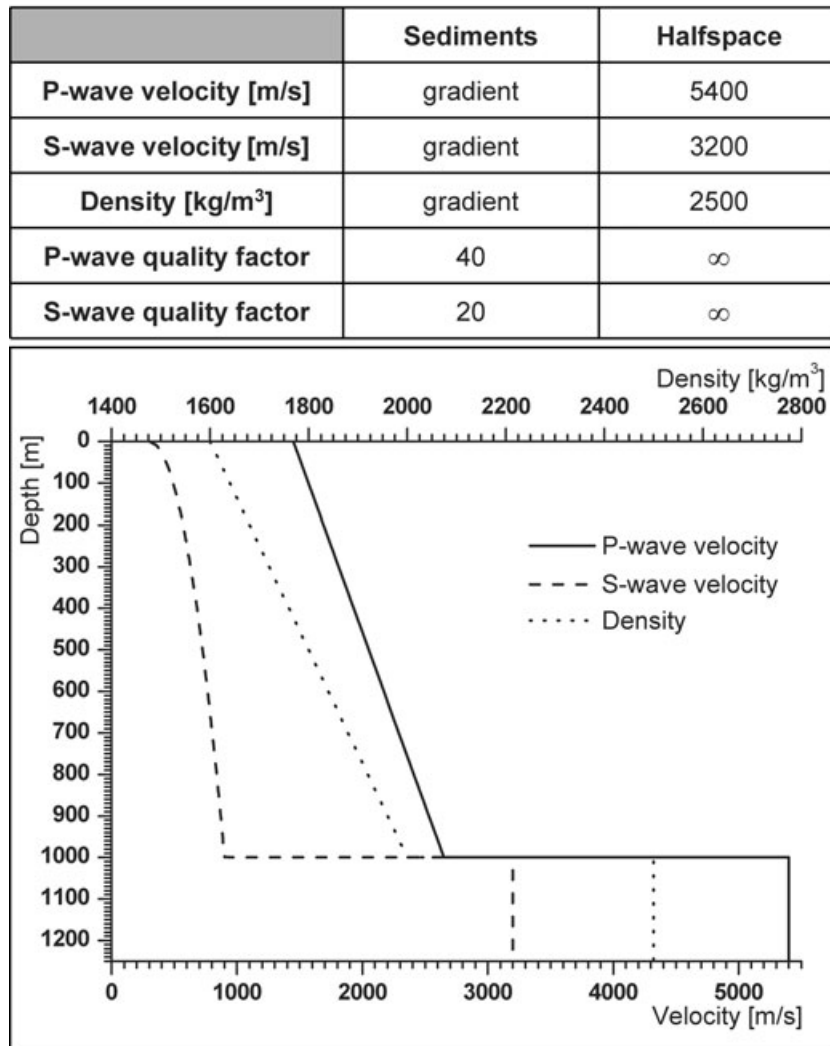


**Figure 23.** Material parameters in the computational model of the Grenoble valley.

instability in the considered problem configurations in the practically sufficient long time windows. However, as already noted in the section on the algorithmically minimal zone, some slight but evident numerical noise appeared in all simulations. Therefore, we tried to modify the transition zone by adding an averaging zone (Fig. 5) in which ‘pure’ FD values and ‘pure’ FE values are replaced by weighted-averages of the FD and FE values. In this sense the averaging zone acts as a smoothing zone.

A series of numerical tests was performed for several canonical problem configurations:

- (1) Unbounded homogeneous space, US, Fig. 6.
- (2) Homogeneous half-space with a planar free surface, FS, Fig. 11.
- (3) Convergence test, Fig. 14.
- (4) Planar contact of two homogeneous half-spaces, Fig. 16.
- (5) Dynamically rupturing planar fault near the FD–FE transition zone, Fig. 18.

### 6.1 Unbounded homogeneous space

Fig. 6 shows two configurations for tests in an unbounded homogeneous elastic space. The US-12 and US-18 configurations differ in the numbers of grid spacings applied to sample the minimum wavelength. 12 grid spacings per minimum wavelength are applied in the FE region in the US-12 configuration whereas 18 grid spacings per minimum wavelength are applied in the US-18 configuration. 6 and 9 grid spacings per minimum wavelength are applied in the FD regions in the two configurations, respectively. In both configurations a point double-couple source was considered in the FE region. Regularly spaced ( $h_{FD}$ ) receiver positions were chosen along a profile extending from the FE region through the FD–FE transition zone into the FD region.

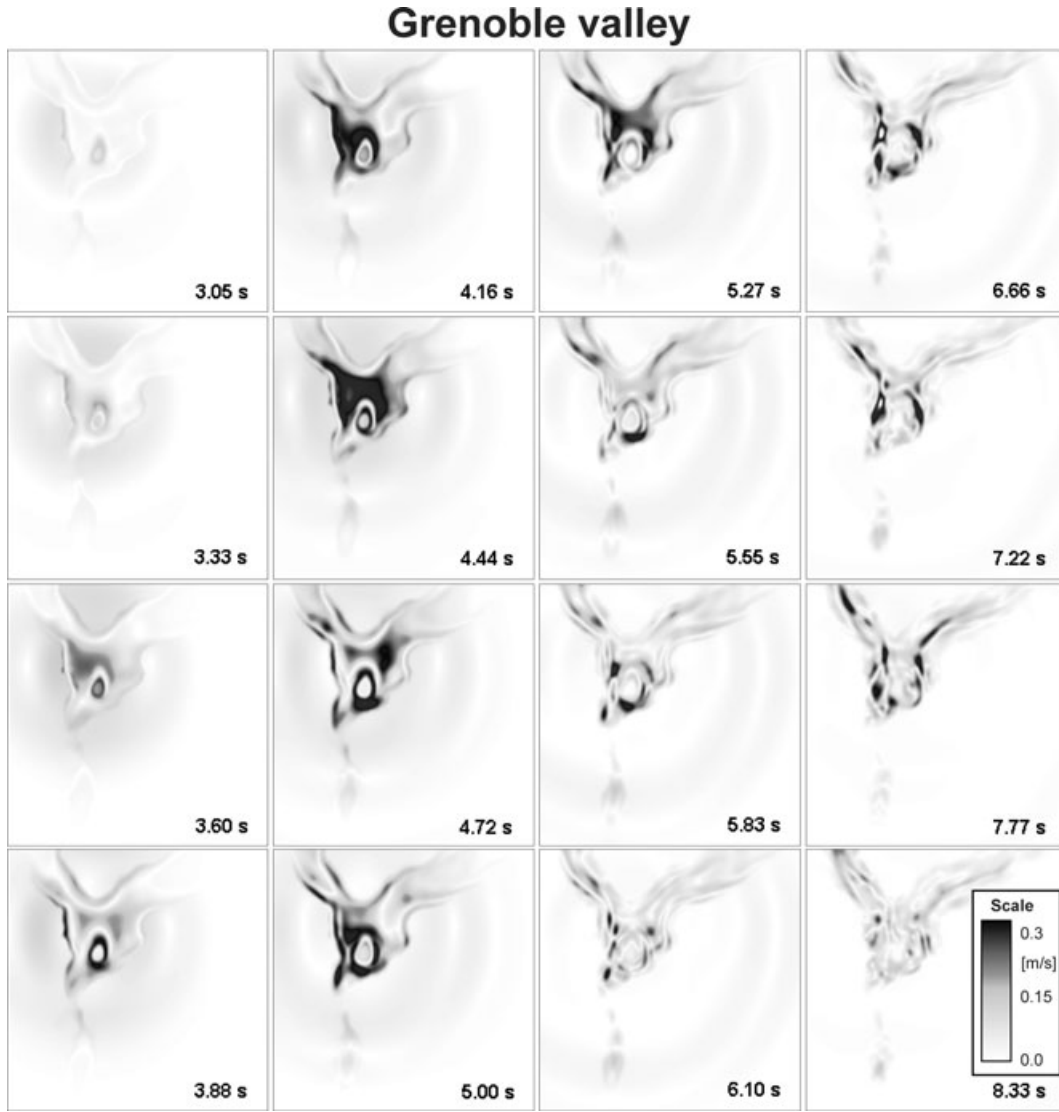


**Figure 24.** Sequence of the wavefield snapshots for the simulated thrust earthquake beneath the Grenoble valley. The grey scale indicates the absolute value of the horizontal component of the particle velocity at the free surface.

For both problem configurations in Fig. 6 we performed numerical simulations for four different FD–FE transition zones, see Fig. 7. The first transition zone, indicated by  $B = 0$  in Fig. 7, corresponds to the algorithmically minimal transition zone with no averaging zone AZ. Three other transition zones, indicated by  $B = 1, 2, 3$  in Fig. 7, differ from each other in the thickness of the averaging zone AZ.

$P$ -wave velocity in the elastic medium is  $5196 \text{ m s}^{-1}$ ,  $S$ -wave velocity  $3000 \text{ m s}^{-1}$  and density is  $2700 \text{ kg m}^{-3}$ . The source time function used is Gabor signal, see Fig. 8,

$$s(t) = \exp \left\{ - \left[ \omega_p(t - t_s) / \gamma_s \right]^2 \right\} \cos \left[ \omega_p(t - t_s) + \Theta \right], \quad (47)$$

with  $\omega_p = 2\pi f_p$ ,  $t \in [0, 2t_s]$  and  $t_s = 0.45\gamma_s/f_p$ . Here,  $\gamma_s$  controls the width of the signal and  $\Theta$  is a phase shift. For certain values of  $\gamma_s$  and  $\Theta$ ,  $f_p$  can be a dominant frequency. The signal and focal parameters of the double-couple point source are given in Table 1.

Results of the numerical tests are summarized in Figs 9 and 10, where the FD–FE hybrid synthetics are compared with those obtained by the discrete-wavenumber method (DWN; Bouchon 1981; Coutant 1989). The synthetics obtained for the algorithmically minimal transition zone are shown together with the DWN synthetics in the top panels. Slight differences are evident behind the main wave group at almost all receiver positions. The synthetics obtained for the  $B = 1$  transition zone are shown together with the DWN synthetics in the middle panels. The FD–FE and DWN synthetics practically coincide within the thickness of the line. All four configurations ( $B = 0, 1, 2, 3$ ) are summarized in the bottom panels where the envelope and phase misfits of the FD–FE solutions relative to the DWN solutions are displayed for all receiver positions. The envelope and phase misfits were calculated according to Kristekova *et al.* (2006). The envelope and phase misfits clearly show that the accuracy of the algorithmically minimal transition FD–FE zone considerably differs from the accuracy of the three other tested transition zones. At the same time, the envelope and phase misfits for the transition zones with the averaging ( $B = 1, 2, 3$ ) are comparable and smaller than 0.5 per cent. This lead us to conclusion that the smallest possible thickness of the averaging zone ( $B = 1$ ) yields sufficiently

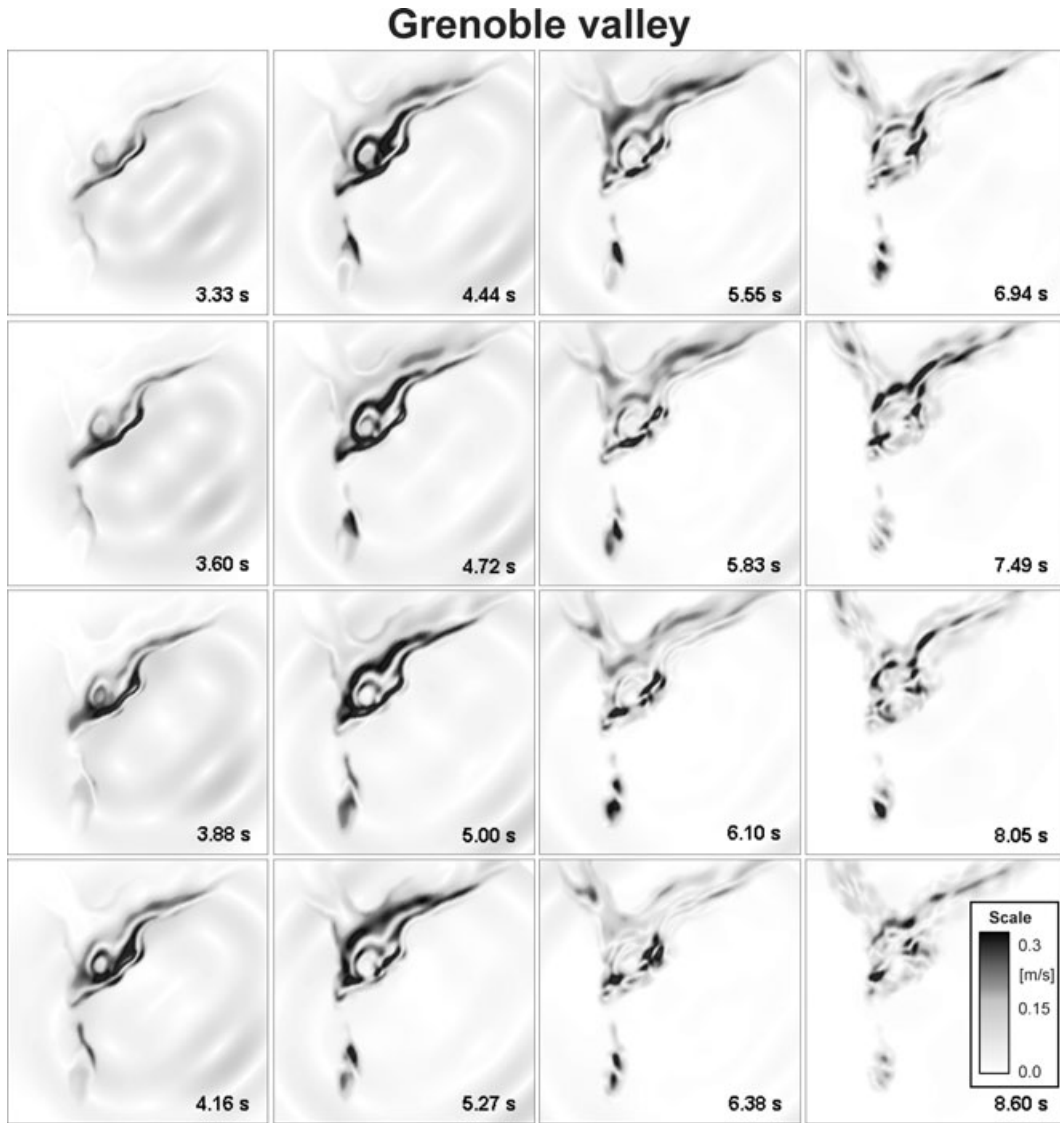


**Figure 25.** Sequence of the wavefield snapshots for the simulated strike-slip earthquake near the Grenoble valley. The grey scale indicates the absolute value of the horizontal component of the particle velocity at the free surface.

accurate results with both levels of spatial grid sampling. As expected, the denser spatial grid sampling in the US-18 simulations yields slightly smaller misfits compared to those in the US-12 simulations.

Let us note that a small spatial ‘gap’ visible in the top and middle panels between synthetics for the U and V components is due to the fact that the U and V grid positions in the staggered FD grid are shifted by  $h_{FD}/2$  relative to the line of the receiver profile extending from the conventional FE grid positions. Because the DWN synthetics were calculated for the exact FD grid positions, the comparison of the FD–FE and DWN solutions is not affected.

The envelope and phase misfits are largest for the V component. This is because the misfits are scaled with respect to the maximum displacement-component amplitude. In the considered problem configuration the maximum amplitude is in the V component.

## 6.2 Homogeneous half-space with a planar free surface

Fig. 11 shows two problem configurations, FS-12 and FS-18. They are similar to the US-12 and US-18 configurations. The difference between the US and FS configurations is that the top side of the FE region as well as the receiver profiles are located directly at the free surface in the FS configurations. The purpose of this choice was to verify behaviour of the FD–FE transition zone in interaction with the planar free surface. The configurations with the free surface can be considered to be more stringent tests for the behaviour of the FD–FE transition zones compared to those in the unbounded homogeneous space. The reasons for this are both the physical effect of the free surface on the

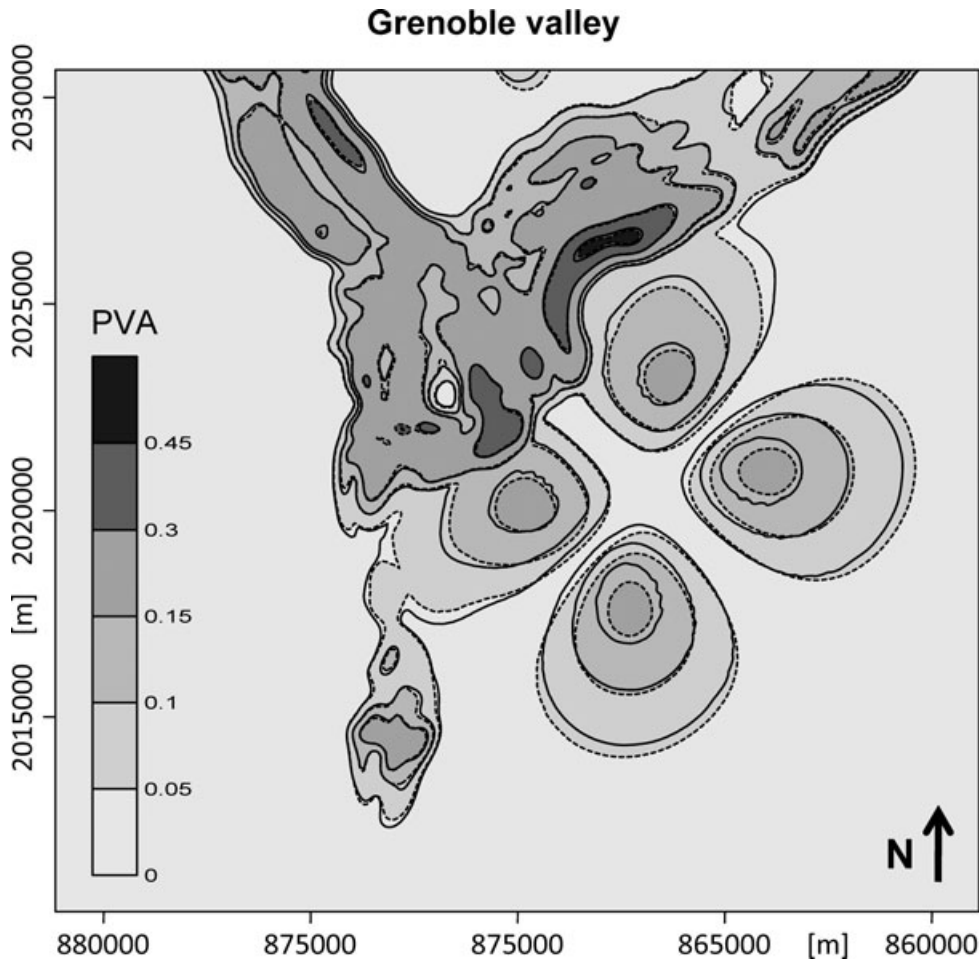


**Figure 26.** Spatial distribution of PVA at the free surface for the vertical- and dipping-fault events. Solid line is used for the PVA isolines for the dipping-fault event, dashed lined for the vertical-fault event.

wavefield and application of the spatially asymmetric interpolation formulas for situations labelled b and c in Fig. 4. As in the case of the US configurations, we investigated four different FD–FE transition zones, see Fig. 7.

Results of the numerical tests are summarized in Figs 12 and 13, where the FD–FE hybrid synthetics are compared with those obtained by the DWN method. The structure of Figs 12 and 13 is the same as that of Figs 9 and 10. It is clear from Figs 12 and 13 that the addition of the averaging zone considerably improves the level of accuracy. At the same time, the envelope and phase misfits for the transition zones with the FD–FE averaging ( $B = 1, 2, 3$ ) are comparable and smaller than 1.0 per cent. This lead us to conclusion that the smallest possible thickness of the averaging zone ( $B = 1$ ) yields sufficiently accurate results with both levels of spatial grid sampling. Again, as expected, the denser spatial grid sampling in the FS-18 simulations yields slightly smaller misfits compared to those in the FS-12 simulations.

### 6.3 Convergence test

The problem configuration is shown in Fig. 14 and is very similar to that of the US-12 for the unbounded homogeneous test (Fig. 6). The purpose of this series of simulations is to check the convergence of the FD–FE transition zone. We consider a fixed physical size of the cube FE region in a homogeneous unbounded medium. A point double-couple source is located at the centre of the FE region. The source–time function and the focal parameters are the same as in the previous simulations. Three receiver positions are at fixed physical positions with respect to the FE region. One, R1, is located in-between the source plane and FE Dirichlet boundary, the second, R2, is exactly at the FE Dirichlet boundary, and the third, R3, is in the FD region. Seven discretizations were considered starting with six elements per minimum wavelength and ending with 24 elements per minimum wavelength. Correspondingly, 3–12 grid spacings were applied in the FD grid. A physical size of the FD–FE transition zone as well as the element size for each of the seven discretization is illustrated in Fig. 14.

Fig. 15 compares results obtained with all the used discretizations in terms of the envelope misfits calculated relative to the exact solutions for three displacement components at the considered receiver positions. Envelope misfits are shown as functions of the number of

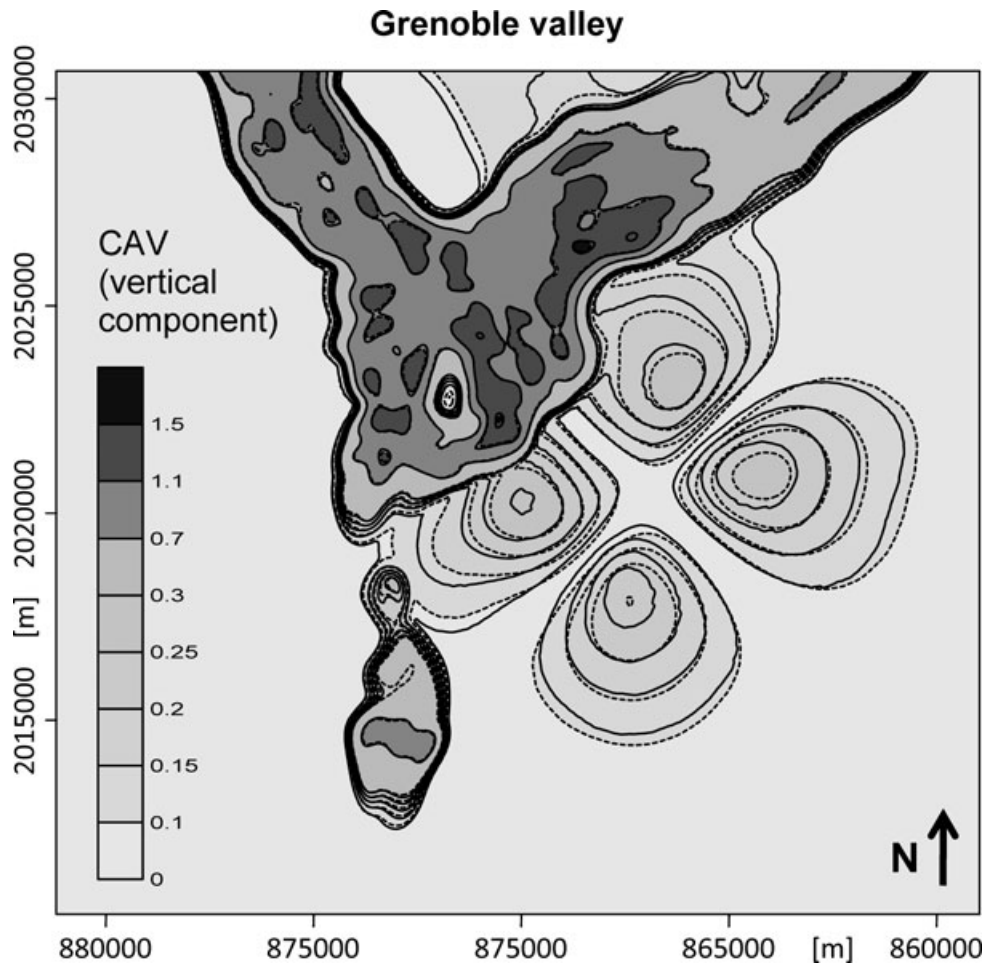


**Figure 27.** Spatial distribution of CAV at the free surface for the vertical- and dipping-fault events. Solid line is used for the CAV isolines for the dipping-fault event, dashed lined for the vertical-fault event.

elements per minimum wavelength. It is clear from the figure that the envelope misfits are sufficiently small—less than 1.0 per cent for all discretizations except the coarsest one. The rate of convergence is approximately 2.

Note that relatively small envelope misfit even for the coarsest discretization should not be surprising given the broad spectrum of the source–time function (Fig. 8) and the fact that six elements sample the minimum wavelength. The broad spectrum also explains why we do not see effect of the grid dispersion—all three receivers are relatively close to the source and the source discretization effect can dominate the grid dispersion at small distances. We should not place receivers farther because the effect of large distances would mask the behaviour of the FD–FE transition zone.

Let us note that the phase misfits between the FD–FE and exact solutions for all discretizations are smaller than the phase misfits between two identical signals shifted in time by one time step. Consequently, the phase misfits cannot be used to analyse the convergence.

#### 6.4 Planar contact of two homogeneous half-spaces

It is also important to check the behaviour of the FD–FE transition zone in a configuration with a material interface. Fig. 16 shows such a configuration. A planar material interface between two homogeneous elastic half-spaces intersects the FE region and thus also the FD–FE transition zone. The cube FE region is centred around a square of the planar interface. As in the previous simulations, the wavefield is due to a point double-couple source that is located in a stiffer half-space and inside the FE region. Receiver positions are along a profile in the softer half-space, two grid spacings ( $2h_{FD}$ ) away from the material interface. The receiver profile extends from the FE region through the FD–FE transition zone into the FD region. The source time function and focal parameters are the same as in the previous tests. The simulation was performed only for the  $B = 1$  transition zone.

The FD–FE hybrid synthetics for the considered problem configuration are compared with the DWN synthetics in Fig. 17. The three displacement components of the synthetics are shown for all regularly spaced ( $5h_{FD}$ ) positions along the receiver profile. The bottom panel of the figure shows the envelope and phase misfits between the FD–FE and DWN synthetics. It is clear that the level of agreement

between the FD–FE and DWN synthetics is very good. The envelope misfits are smaller than 1.0 per cent and phase misfits are smaller than 0.5 per cent.

### 6.5 Dynamically rupturing planar fault near the FD–FE transition zone

As we already pointed out, one important application of the hybrid FE–FD method is the comprehensive modelling of earthquake motion with a dynamically rupturing fault. If we place the rupturing fault surface inside the FE region then the question arises how large the FE region should be. In other words, how far should the FD–FE transition zone be placed from the fault in order to avoid a numerical effect of the transition zone on the rupture propagation. Therefore, we performed a series of numerical tests for the dynamically propagating rupture.

The geometrical configuration is indicated in Fig. 18. We performed numerical simulations for 6 different distances between the rupturing fault plane and FD–FE transition zone. The fault is located in a homogeneous elastic medium. Material and computational parameters of the simulations are given in Table 2. A linear slip-weakening friction law is assumed. The initial normal and shear tractions, as well as all constitutive parameters are spatial constants. The rupture propagation is initialized in a circular initialization zone using the initial shear traction larger by 0.5 per cent than the yield traction. Constitutive parameters used in the simulations are given in Table 3. Fig. 19 shows three selected receiver positions on the fault plane. One receiver position, R1, was chosen to record a pure in-plane mode of the rupture propagation. The receiver position R2 was chosen for an antiplane mode, and R3 near the line of the rupture front splitting.

The non-filtered slip-rate time histories obtained at the receiver positions R1–R3 for the six different distances between the fault plane and FD–FE transition zone are summarized in Fig. 20. As we expected, the minimum possible distance of just one FE grid spacing,  $\delta = h_{\text{FE}}$ , is not sufficient. The simulation with  $\delta = 9 h_{\text{FE}}$  yields slip rate that is hard to distinguish from the slip rate obtained with  $\delta = 21 h_{\text{FE}}$ . As it is clear from Fig. 20, the latter solution can be considered as an acceptable FE solution for the chosen computational parameters.

In the slip histories at R2 we can easily recognize the presence of a disturbance which shifts in time with the increasing distance  $\delta$ . The only interpretation we were able to find is that the disturbance is due to a ‘reflection’ from the FE Dirichlet boundary (see Fig. 18). Practically taken, the disturbance does not pose a problem because it is the high-frequency disturbance beyond the frequency up to which the simulation can be considered as acceptably accurate. We point out that the slip-rate histories shown in Fig. 20 are not filtered.

## 7 ILLUSTRATIVE NUMERICAL SIMULATIONS FOR TWO HYPOTHETICAL EVENTS NEAR THE GRENOBLE VALLEY

Based on investigations of the historical earthquake activity and tectonic situation of the Grenoble valley by Gamond (1994) and Thouvenot (1996), Cotton *et al.* (1998) performed numerical simulations of the earthquake motion in the Grenoble valley for two hypothetical earthquakes. One was a thrust event beneath Grenoble, the other a strike-slip faulting in the Belledonne Massif. In both cases Cotton *et al.* (1998) used the fourth-order velocity–stress staggered-grid FD scheme and modelled the earthquake sources as kinematic point sources.

Here we consider a finite size of the ruptured area and spontaneous rupture propagation to model the two hypothetical events. Parameters of the same dynamic model for both events were suggested by Michel Bouchon and Pierre-Yves Bard (LGIT, Université Joseph Fourier, Grenoble). They are: the initial traction in the horizontal in-plane direction 10 MPa, initial traction in the horizontal antiplane direction 0 MPa, initial normal traction –17 MPa, static and dynamic coefficients of friction 0.7 and 0.235, respectively, and critical distance 0.1 m assuming a linear slip-weakening friction law. In order to produce slip equivalent to a  $M_W = 5.3$  earthquake the ruptured area was restricted to approximately  $4 \times 2$  km by a continuous increase of the values of the static and dynamic coefficients of friction. The hypocentre was located at the centre of the ruptured area. The initialization zone was a circle. The in-plane shear initial traction inside the circular initialization zone with the 500 m diameter was 2.5 per cent larger than the static traction.

The geometrical configurations for the two events are shown in Figs 21 and 22, respectively. The rupturing area of the fault is located inside the relatively small FE box. The major part of the domain is covered by the FD grid. This hybrid or combined coverage of the computational domain makes the simulation computationally considerably more efficient compared to the simulation with the FE grid covering the whole domain. The material parameters of the structural model are specified in Fig. 23. The computational parameters were chosen such that the simulation should be sufficiently accurate up to approximately 7.6 Hz in the bedrock and 0.7 Hz in the sediments near the free surface.

Results of the numerical simulations for the two events are illustrated in Figs 24 and 25. The two sequences of snapshots clearly indicate seismic waves radiated from the rupturing fault and the corresponding seismic motion outside the valley as well as the penetration of the seismic waves into the sedimentary body at earlier times of the simulation. Due to the relatively large impedance contrast between the sediments and bedrock, the seismic energy is trapped in the sediments at later times, and the motion inside the valley significantly dominates that outside the valley. Snapshots indicate complex wave fields inside the sediments due to the geometrically complicated sediment–bedrock interface. At the same time, the space–time variation of the motion in the valley due to the thrust event considerably differs from that due to the strike-slip event. Clearly, this is a consequence of different geometrical configurations of the valley structure and the rupturing fault.

Obviously, the two simulated motions can be compared in terms of several characteristics of the motion. Those could include time–frequency analysis as well as earthquake-engineering characteristics as Arias intensity and cumulative absolute velocity. The motions due to the dynamic models could be also compared with the motions simulated for point sources equivalent in terms of the scalar seismic moment and focal mechanism. This, however, is not a goal of the just illustrative simulations.

In order to illustrate the possibility to simulate dynamically rupturing dipping fault we considered a fault dipping  $85^\circ$  NE. Except the dipping fault, all other parameters were the same as for the Belledonne strike-slip event. Note that the consideration of the dipping fault would be a major problem for the standard staggered-grid finite-difference scheme on a uniform grid with grid planes parallel to the Cartesian coordinate planes. Fig. 26 shows a distribution of the maximum value of modulus of the vertical component of acceleration, PVA, at the free surface for the vertical and dipping faults. We show the results for the vertical components because the difference between the two events is better seen for them, compared to the horizontal components, both outside and inside the sedimentary valley. Fig. 27 compares cumulative absolute velocities (CAV) at the free surface for the two events. CAV is defined here as

$$CAV = \int_0^{t_0} |a(t)| \, dt, \quad (48)$$

with  $t_0$  being time when the strong motion ceases and  $a(t)$  the vertical acceleration. (In general,  $a(t)$  represents vector of the particle acceleration, see, e.g. Reiter 1990). The effect of the dipping fault is evident but, at the same time, it is clear, that the  $5^\circ$  difference in dip of the fault does not cause considerable difference in the two chosen characteristics.

## 8 CONCLUSIONS

We have developed a new hybrid numerical method for the 3-D viscoelastic modelling of seismic wave propagation and earthquake motion in the heterogeneous medium. The method causally combines the fourth-order velocity–stress staggered-grid FD scheme with the second-order FE method. A major part of the computational domain is covered by the FD grid whereas one or more subdomains are covered by finite elements. The FE subdomains can comprise extended kinematic or dynamic models of the earthquake source or free-surface topography.

The realistic attenuation is incorporated using the rheology of the generalized Maxwell body in definition by Emmerich & Korn (1987). The rheology is strictly equivalent to that of the generalized Zener body—as shown by Moczo & Kristek (2005).

The implemented FE formulation makes use of the concept of the global restoring-force vector which significantly reduces memory requirements compared to the standard formulation based on the global stiffness matrix.

The kinematic source is simulated using the body-force term. For simulation of the spontaneous rupture propagation in the dynamic source model the TSN method is implemented in the FE method.

The key algorithmical part of the causally communicating FD and FE parts of the model is the FD–FE transition zone in which the FD and FE schemes communicate at each time level. Extensive numerical tests led us to define a smooth FD–FE transition zone consisting of the FE Dirichlet boundary, FD–FE averaging zone and FD Dirichlet zone. The smooth transition zone numerically performs better than the algorithmically minimal transition zone which does not include the FD–FE averaging zone.

The developed hybrid method can be applied to a variety of problems related to the numerical modelling of the earthquake ground motion in structurally complex media and particularly in near-surface laterally heterogeneous sedimentary structures including the free-surface topography and the extended kinematic or dynamic earthquake sources. The method can be also useful in the source dynamics studies.

## ACKNOWLEDGMENTS

We thank Michel Bouchon and Pierre-Yves Bard for discussions related to the hypothetical earthquakes near the Grenoble valley, France. We thank Martin Käser for his useful critical review and Jean Virieux for his critical comments. They considerably helped to improve the presentation. This work was supported in part by the Marie Curie Research Training Network SPICE Contract No. MRTN-CT-2003-504267 and VEGA Project 1/4032/07.

## REFERENCES

- Alekseev, A.S. & Mikhailenko, B.G., 1980. The solution of dynamic problems of elastic wave propagation in inhomogeneous media by a combination of partial separation of variables and finite-difference methods, *J. Geophys.*, **48**, 161–172.
- Andrews, D.J., 1973. A numerical study of tectonic stress release by underground explosions, *Bull. seism. Soc. Am.*, **63**, 1375–1391.
- Andrews, D.J., 1976a. Rupture propagation with finite stress in antiplane strain, *J. geophys. Res.*, **81**, 3575–3582.
- Andrews, D.J., 1976b. Rupture velocity of plane strain shear cracks, *J. geophys. Res.*, **81**, 5679–5687.
- Andrews, D.J., 1999. Test of two methods for faulting in finite-difference calculations, *Bull. seism. Soc. Am.*, **89**, 931–937.
- Archuleta, R.J., 1976. Experimental and numerical three-dimensional simulations of strike-slip earthquakes, *PhD thesis*, University of California, San Diego.
- Bouchon, M., 1981. A simple method to calculate Green's functions for elastic layered media, *Bull. seism. Soc. Am.*, **71**, 959–971.
- Bouchon, M. & Coutant, O., 1994. Calculation of synthetic seismograms in a laterally-varying medium by the boundary element—discrete wavenumber method, *Bull. seism. Soc. Am.*, **84**, 1869–1881.
- Chaljub, E., Komatitsch, D., Vilotte, J.P., Capdeville, Y. & Festa, G., 2007. Spectral Element Analysis in Seismology, in *Advances in Wave Propagation in Heterogeneous Earth*, Vol. 48, pp. 365–420, eds Wu, R.-S., Maupin, V. & Dmowska, R., in the series *Advances in Geophysics*, Elsevier/Academic Press, San Diego.
- Cotton, F., Berge, C., Lemeille, F., Pitarka, A., Lebrun, B. & Vallon, M., 1998. Three-dimensional simulation of earthquakes in the Grenoble's basin, in *The Effects of Surface Geology on Seismic Motion*, Vol. 2, pp. 873–878, eds Irikura, K., Kudo, K., Okada, H. & Sasatani, T., Balkema, Rotterdam.
- Coutant, O., 1989. Program of numerical simulation AXITRA. Res. Rep. LGIT (in French), *Université Joseph Fourier*, Grenoble.
- Day, S.M., 1977. Finite element analysis of seismic scattering problems, *PhD dissertation*, University of California, San Diego.
- Day, S.M., 1982. Three-dimensional simulation of spontaneous rupture: the effect of nonuniform prestress, *Bull. seism. Soc. Am.*, **72**, 1881–1902.

- Day, S.M., 1998. Efficient simulation of constant Q using coarse-grained memory variables, *Bull. seism. Soc. Am.*, **88**, 1051–1062.
- de la Puente, J., Käser, M., Dumbser, M. & Igel, H., 2007. An arbitrary high-order discontinuous Galerkin method for elastic waves on unstructured meshes—IV. Anisotropy, *Geophys. J. Int.*, **169**, 1210–1228.
- Emmerich, H., 1989. 2-D wave propagation by a hybrid method, *Geophys. J. Int.*, **99**, 307–319.
- Emmerich, H., 1992. PSV-wave propagation in a medium with local heterogeneities: a hybrid formulation and its application, *Geophys. J. Int.*, **109**, 54–64.
- Emmerich, H. & Korn, M., 1987. Incorporation of attenuation into time-domain computations of seismic wave fields, *Geophysics*, **52**, 1252–1264.
- Fäh, D., 1992. A hybrid technique for the estimation of strong ground motion in sedimentary basins. Diss. ETH Nr. 9767, *Swiss Federal Institute of Technology*, Zürich.
- Fäh, D., Suhadolc, P. & Panza, G.F., 1993. Variability of seismic ground motion in complex media: the case of a sedimentary basin in the Friuli (Italy) area, *J. appl. Geophys.*, **30**, 131–148.
- Frazier, G.A. & Petersen, C.M., 1974. 3-D stress wave code for the Illiac IV, *Systems, Science and Software Report SSS-R-74-2103*.
- Gaffet, S. & Bouchon, M., 1989. Effects of two-dimensional topographies using the discrete wavenumber-boundary integral equation method in P-SV cases, *J. acoust. Soc. Am.*, **85**, 2277–2283.
- Gamond, J.F., 1994. Normal faulting and tectonic inversion driven by gravity in a thrusting regime, *J. Struct. Geol.*, **16**, 1–9.
- Graves, R.W. & Day, S.M., 2003. Stability and accuracy analysis of coarse-grain viscoelastic simulations, *Bull. seism. Soc. Am.*, **93**, 283–300.
- Käser, M. & Dumbser, M., 2006. An arbitrary high-order discontinuous Galerkin method for elastic waves on unstructured meshes—I. The two-dimensional isotropic case with external source terms, *Geophys. J. Int.*, **166**, 855–877.
- Käser, M., Dumbser, M., de la Puente, J. & Igel, H., 2007. An arbitrary high-order discontinuous Galerkin method for elastic waves on unstructured meshes—III. Viscoelastic attenuation, *Geophys. J. Int.*, **168**, 224–242.
- Kawase, H., 1988. Time-domain response of a semi-circular canyon for incident SV, P, and Rayleigh waves calculated by the discrete wavenumber boundary element method, *Bull. seism. Soc. Am.*, **78**, 1415–1437.
- Komatitsch, D., Tsuboi, S. & Tromp, J., 2005. The Spectral-Element Method in Seismology, in *Seismic Earth: Array Analysis of Broadband Seismograms*, Vol. 157, pp. 205–228, eds Levander, A. & Nolet, G., in the series Geophysical Monograph.
- Kristek, J. & Moczo, P., 2003. Seismic wave propagation in viscoelastic media with material discontinuities—a 3D 4th-order staggered-grid finite-difference modeling, *Bull. seism. Soc. Am.*, **93**, 2273–2280.
- Kristek, J. & Moczo, P., 2006. On the accuracy of the finite-difference schemes: the 1D elastic problem, *Bull. seism. Soc. Am.*, **96**, 2398–2414.
- Kristek, J., Moczo, P. & Archuleta, R.J., 2002. Efficient methods to simulate planar free surface in the 3D 4th-order staggered-grid finite-difference schemes, *Studia Geophys. Geod.*, **46**, 355–381.
- Kristekova, M., Kristek, J., Moczo, P. & Day, S.M., 2006. Misfit criteria for quantitative comparison of seismograms, *Bull. seism. Soc. Am.*, **96**, 1836–1850.
- Kummer, B., Behle, A. & Dorau, F., 1987. Hybrid modelling of elastic-wave propagation in two-dimensional laterally inhomogeneous media, *Geophysics*, **52**, 765–771.
- Lecomte, I., Gjovystdal, H., Maaø, F., Bakke, R., Drottning, A. & Johansen, T.-A., 2004. Efficient and flexible seismic modelling of reservoirs: the HybriSeis concept, *Leading Edge*, **23**, 432–437.
- Ma, S., Archuleta, R.J. & Liu, P., 2004. Hybrid modeling of elastic P-SV wave motion: a combined finite-element and staggered-grid finite-difference approach, *Bull. seism. Soc. Am.*, **94**, 1557–1563.
- Mikhailenko, B.G. & Korneev, V.I., 1984. Calculation of synthetic seismograms for complex subsurface geometries by a combination of finite integral Fourier transform and finite-difference techniques, *J. Geophys.*, **54**, 195–206.
- Moczo, P. & Kristek, J., 2005. On the rheological models used for time-domain methods of seismic wave propagation, *Geophys. Res. Lett.*, **32**, L01306.
- Moczo, P., Bystrický, E., Kristek, J., Carcione, J.M. & Bouchon, M., 1997. Hybrid modeling of P-SV seismic motion at inhomogeneous viscoelastic topographic structures, *Bull. seism. Soc. Am.*, **87**, 1305–1323.
- Moczo, P., Kristek, J., Vavryčuk, V., Archuleta, R.J. & Halada, L., 2002. 3D heterogeneous staggered-grid finite-difference modeling of seismic motion with volume harmonic and arithmetic averaging of elastic moduli and densities, *Bull. seism. Soc. Am.*, **92**, 3042–3066.
- Moczo, P., Kristek, J. & Galis, M., 2004. Simulation of planar free surface with near-surface lateral discontinuities in the finite-difference modeling of seismic motion, *Bull. seism. Soc. Am.*, **94**, 760–768.
- Moczo, P., Kristek, J., Galis, M., Pazak, P. & Balazovjech, M., 2007a. The finite-difference and finite-element modeling of seismic wave propagation and earthquake motion, *Acta Phys. Slovaca*, **57**, 177–406. (Available at <http://www.physics.sk/aps/pub.php?y=2007&pub=aps-07-02>)
- Moczo, P., Robertsson, J.O.A. & Eisner, L., 2007b. The finite-difference time-domain method for modeling of seismic wave propagation, in *Advances in Wave Propagation in Heterogeneous Earth*, Vol. 48: *Advances in Geophysics*, pp. 421–516, eds Wu, R.-S., Maupin, V. & Dmowska, R., Elsevier/Academic Press, San Diego.
- Ohtsuki, A. & Harumi, K., 1983. Effects of topography and subsurface inhomogeneities on seismic SV waves, *Earthq. Eng. Struct. Dyn.*, **11**, 441–462.
- Reiter, L., 1990. *Earthquake Hazard Analysis. Issues and Insights*, Columbia University Press, New York.
- Robertsson, J.O.A., 1996. A numerical free-surface condition for elastic/viscoelastic finite-difference modeling in the presence of topography, *Geophysics*, **61**, 1921–1934.
- Rovelli, A., Caserta, A., Malagnini, L. & Marra, F., 1994. Assessment of potential strong ground motions in the city of Rome, *Annali di Geofisica*, **37**, 1745–1769.
- Shtivelman, V., 1984. A hybrid method for wave field computation, *Geophys. Prospect.*, **32**, 236–257.
- Shtivelman, V., 1985. Two-dimensional acoustic modelling by a hybrid method, *Geophysics*, **50**, 1273–1284.
- Stead, R.J. & Helmberger, D.V., 1988. Numerical-analytical interfacing in two dimensions with applications to modeling NTS seismograms, in *Scattering and Attenuation of Seismic Waves*, pp. 157–193, eds Aki, A. & Wu, R.-S., Birkhauser, Basel.
- Thouvenout, F., 1996. Aspects géophysiques et structuraux des Alpes occidentales et de trois autres orogènes (Atlas, Pyrénées, Oural), *Université Joseph Fourier*, Grenoble, pp. 378.
- Tromp, J., Komatitsch, D. & Liu, Q., 2008. Spectral-element and adjoint methods in seismology, *Commun. Computat. Phys.*, **3**, 1–32.
- Van den Berg, A., 1984. A hybrid solution for wave propagation problems in regular media with bounded irregular inclusions, *Geophys. J. R. astr. Soc.*, **79**, 3–10.
- Zahradník, J. & Moczo, P., 1996. Hybrid seismic modeling based on discrete-wavenumber and finite-difference methods. *PAGEOPH*, **148**, 21–38.